

# Physics of the Earth's interior

A.P. van den Berg

January 6, 2016

## Contents

<b>1</b>	<b>Introduction</b>	<b>2</b>
<b>2</b>	<b>Global internal structure and temperature of the Earth</b>	<b>4</b>
2.1	Early models of the Earth's density . . . . .	4
2.2	The moment of inertia of a spherically symmetric density distribution . . . . .	5
2.3	Density, gravity and pressure in the Earth . . . . .	7
2.4	Gravity field of a mass distribution . . . . .	8
2.4.1	Problem section: spherically symmetric density distributions and corresponding gravity fields . . . . .	10
2.5	The gravity and pressure field for parameterized density models with self-gravitation	12
2.6	The pressure effect on density . . . . .	15
2.6.1	Introduction . . . . .	15
2.6.2	Parameterization of the bulkmodulus . . . . .	16
2.6.3	Adiabatic density distribution . . . . .	20
2.7	Current density models . . . . .	22
2.8	Earth's chemical composition . . . . .	23
2.9	Phase transitions as anchor points of the geotherm . . . . .	26
<b>3</b>	<b>Thermal state of the Earth</b>	<b>30</b>
3.1	Introduction . . . . .	30
3.2	Earth's heat output . . . . .	31
3.3	The Earth's energy budget and energy transport mechanisms . . . . .	33
3.4	Internal heating by natural radioactive decay . . . . .	34
3.4.1	Radiogenic heating in a chondritic earth . . . . .	34
3.4.2	Heat production rates in representative rocks . . . . .	35
3.5	Thermal evolution models . . . . .	39
3.5.1	Parameterized evolution models . . . . .	39
3.5.2	Convection models . . . . .	41
3.5.3	The role of solid state phase transitions in convective heat transport . . . . .	48
	<b>References</b>	<b>51</b>

<b>A Concepts of thermal energy transport</b>	<b>54</b>
A.1 Transport equations . . . . .	54
A.2 Thermal energy conservation applied to a cooling body . . . . .	55
A.3 The adiabatic temperature profile of a convecting layer . . . . .	56

## 1 Introduction

The internal constitution of the Earth has been investigated systematically from the nineteenth century on. With the advent of seismological instrumentation for the registration of tele-seismic events, by the end of that century, the main tool for obtaining direct information about distribution of the material properties controlling seismic wave propagation became available. Before this, mainly global properties could be determined from gravity and magnetic field observations, astronomical data and indications about the heatflow from the Earth's interior. As a result of the early seismological investigations the main internal structure of the Earth was revealed within the first few decades of the twentieth century with the discovery of the earth's core in 1906 by Oldham and Gutenberg (1912) and the solid inner core in 1936 by Lehmann.

From the radial distribution of the seismic velocity profile, obtained by processing the tables of traveltimes versus epicentral distance, Williamson and Adams (1923) made a first estimate of the density profile for a compressible homogeneous mantle model, consistent with the total mass of the Earth and obtained at the same time strong indication for a high density core, compositionally distinct from the mantle.

Bullen (1975) further refined the analysis and showed the assumption of a homogeneous mantle to be inconsistent with the known moment of inertia of the Earth. In the 1940s and 1950s he introduced a global division of the Earth in concentric shells, labelled A through G, ranging from the Earth's crust (A), bounded by the Moho discontinuity, to the inner core (G). Region C between, roughly 400km and 900km, characterized by rapid increase of the seismic velocities, was identified by Bullen as a transition region between the upper mantle region B and a homogeneous lower mantle, region D. The deduced inhomogeneity of the mantle was projected by Bullen in this C region. E through G were used to label subdivisions of the core. Region E indicated the liquid, adiabatic outer core, F a transition region between inner and outer core and G the solid inner core. Birch (1952) published improved equations of state, based on finite-strain theory, thereby giving a more firm physical basis to interpretation of available data in terms of a compressible medium.

In the second half of the twentieth century the resolution and accuracy of the models were further improved using continuously improved seismological observations and a growing data set. It also became possible to obtain independent information about the radial density distribution from spectral analysis of radial eigen-vibrations of the Earth after very large earthquakes. This development resulted in the publication of the Preliminary Reference Earth Model (PREM) (Dziewonski and Anderson, 1981) which still serves as a global reference.

The improved seismological models indicated that the continuous rapid velocity increase in the transition zone (C) was actually a succession of several abrupt changes, confirming radial inhomogeneity in mineral phase and possibly in chemical composition of the mantle.

From geological and cosmochemical arguments a probable composition of the Earth had been derived consisting of a mantle with major element composition dominated by magnesium-iron silicates and an iron-nickel core with a small amount of lighter elements mixed in, most likely including mainly sulphur. In the 1960s this resulted in the definition of a so-called pyrolytic composition of the mantle by Ringwood which could explain the main mantle petrological observations regarding the complementary nature of basalts and ultra mafic mantle rocks found in ophiolites, kimberlites and mantle peridotite bodies (Ringwood, 1975).

In experimental high-pressure and temperature work on the candidate mantle materials a series of phase transitions were found at pressure and temperature values relevant for the Earth's mantle which could be related to the seismic discontinuities revealed by the seismological data. From

these the most prominent at approximately 410 and 660 km depth were identified as the phase transition of the olivine component  $(\text{Mg, Fe})_2\text{SiO}_4$  of the pyrolitic mantle to a denser wadsleyite crystal structure and, at 660 km, a transition (dissociation) from a  $\gamma$ -spinel (known as ringwoodite) structure to a two-phase assemblage, post-spinel, i.e. magnesium-iron perovskite,  $(\text{Mg, Fe})\text{SiO}_3$  and wüstite  $(\text{Mg, Fe})\text{O}$ .

It was also found that the 660 km boundary corresponds to an endothermic phase transition which would have implications for large scale circulation in the mantle, leading to long-standing speculations about the degree of layering in mantle convection (Christensen and Yuen, 1985, Albarede and van der Hilst, 2002), <http://www.mantleplumes.org>.

A more recent development in this area is the discovery of a new phase transition of magnesium-perovskite to a denser form for pressure temperature conditions, approximately 125 GPa 2500 K, relevant for the D'' layer close to the core-mantle boundary (Lay et al., 2005, van der Hilst et al., 2007).

In the following sections the density distribution in the Earth's interior is treated in relation to the gravity field and internal pressure distribution of a self-gravitating compressible planet model and the link is shown with results from theoretical mineral physics and high pressure-temperature experimental data for mantle materials.

## 2 Global internal structure and temperature of the Earth

To understand the Earth's internal dynamics and evolution we need to know it's internal structure and material properties. What do we know about Earth's global internal structure?

For a substance of given chemical composition, the material properties are determined by temperature and pressure. A full understanding of the Earth's internal dynamics therefore requires that we know the internal distribution of composition, temperature and pressure. The internal pressure distribution is directly linked with the Earth's own internal gravity field and density distribution because the local pressure gradient equals the local gravity acceleration times the density (see problem 6). In section 2.3 density, gravity and pressure are treated together in a consistent way.

If the internal pressure distribution is known we can relate sharp transitions in the physical parameters as shown in the PREM model, illustrated in Fig. 1, to phase transitions, solid-solid or solid-liquid, in the Earth's deep interior.

Phase transitions in 'candidate' materials for the Earth's interior are investigated under high pressure and temperature conditions in HPT laboratory experiments.<sup>1</sup> Using theoretical mineral physics models the complete mineral phase diagram of mantle silicates can, in principle, be constructed from a limited set of experimental data (Stixrude and Lithgow-Bertelloni, 2005, Jacobs and de Jong, 2007). To constrain the possible candidate materials we also need to know the internal distribution of the Earth's chemical composition. Such composition models are derived from geological evidence and cosmochemical considerations.

### 2.1 Early models of the Earth's density

The total Earth mass  $M_{\oplus}$  and average density  $\langle \rho \rangle$  were not known before independent measurement of Newton's gravitational constant by Cavendish, (see section 2.3). When the average density had been determined as approximately  $5.5 \cdot 10^3 \text{ kgm}^{-3}$  it became clear, from the lower density of surface rocks of around  $2.7 \cdot 10^3 \text{ kgm}^{-3}$ , that the Earth's interior must consist of higher density material.

Besides the mass or average density the (average) moment of inertia  $I$  (defined in section 2.2) provides a constraint on the radial distribution of density.

These two integral parameter values have been applied in several two-parameter models for the radial density distribution of the Earth. At the end of the nineteenth century Wiechert assumed that the compressibility of Earth materials would be negligible to first approximation and that Earth's high mean density was due to a dense, probably metallic, core. He assumed an iron core based on astronomical evidence of high iron content of the sun's outer layers (see also section 2.8).

Wiechert considered in particular layered spherically symmetric models consisting of two uniform layers, core and mantle. Since the radius of the Earth's core had not yet been determined by seismology, Wiechert used the core radius  $R_c$  and density  $\rho_c$  as unknown parameters to be determined from the known data. Wiechert assumed the density of the mantle to be  $\rho_m = 3.2 \cdot 10^3 \text{ kgm}^{-3}$  and using known values for  $M$  and  $I$  he derived for the radius of the core  $R_c/R = 0.779$  corresponding to a mantle depth of about 1400 km and a core density  $\rho_c = 8.2 \cdot 10^3 \text{ kgm}^{-3}$ . This model is investigated in problem 3.

Later, after  $R_c/R = 0.545$  had been determined using seismic data, Jeffreys substituted the known value of the core radius and derived for the mantle and core densities  $\rho_c = 12.6 \cdot 10^3 \text{ kgm}^{-3}$  and  $\rho_m = 4.14 \cdot 10^3 \text{ kgm}^{-3}$  (Bullen, 1975). This model is investigated in problem 4.

---

<sup>1</sup>Deep Earth pressure and temperature conditions can be produced in a Diamond Anvil Cell (DAC), see [http://en.wikipedia.org/wiki/Diamond\\_anvil\\_cell](http://en.wikipedia.org/wiki/Diamond_anvil_cell).

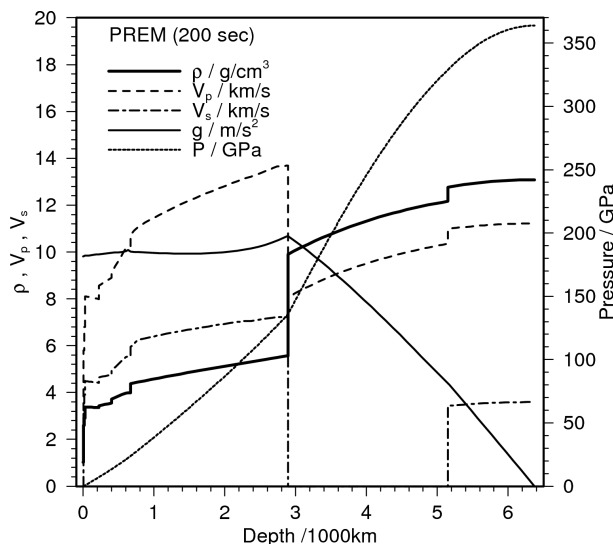


Figure 1: Radial (depth) distribution of density  $\rho$ , seismic velocities  $v_p$  and  $v_s$ , gravity acceleration  $g$  and pressure  $P$  in the PREM model (Dziewonski and Anderson, 1981).

## 2.2 The moment of inertia of a spherically symmetric density distribution

The moment of inertia  $I$  of a point mass of mass  $m$ , with respect to a given rotation axis is defined as  $I = md^2$  where  $d$  is the distance from the point mass to the axis. This quantity relates the angular velocity  $\omega$ , about the rotation axis, to the angular momentum  $J$ , of the point mass, in  $J = I\omega$ . This is an analogous relation as the one between the linear momentum  $p$  and the linear velocity  $v$ ,  $p = mv$ . For an extended mass distribution in a volume  $V$ , a moment of inertia tensor,  $I_{ij}$ , relating the angular momentum vector  $\mathbf{J}$  to the rotation vector  $\mathbf{\Omega}$  can be defined as  $J_i = I_{ij}\Omega_j$ , where the summation convention for repeated indices is implied. This tensor is described by a  $3 \times 3$  matrix defined by volume integration over point masses in the volume. Here we only consider spherically symmetric mass distributions where the moment tensor is isotropic,  $I_{ij} = I\delta_{ij}$ , with scalar coefficient  $I$ .<sup>2</sup> In simple terms, the moment of inertia is the same for any rotation axis through the centre of the spherically symmetric body.

For a spherically symmetric body of finite volume, the scalar moment of inertia is defined as a volume integral over point masses,  $I = \int_V \rho d^2 dV$ <sup>3</sup>.

The moment of inertia of a spherically symmetric density distribution is often expressed in terms of the total mass  $M$ , the outer radius  $R$  and a prefactor  $f$  as,

$$I = fMR^2 \quad (1)$$

We have seen that the planetary mass and surface density were used to constrain models for the interior density distribution. These models are further constrained by the planets moment of

<sup>2</sup> $\delta_{ij}$  is the Kronecker delta, i.e.  $\delta_{ij} = 1$  for  $i = j$  and zero otherwise.

<sup>3</sup>The moment of inertia  $I$  can be determined from Earth's global gravity field and the precession rate of the rotation axis determined from astronomical data, see Bullen, *The Earth's density*, 1975.

inertia  $I$  that can be determined from (satellite) geodetic and astronomical observations. For Earth the following values for the total mass and moment of inertia prefactor have been found,

$$M = 5.97 \cdot 10^{24} \text{ kg}, \quad I = 0.3307MR^2 \quad (2)$$

where  $R = 6371$  km is the mean radius. The observed moment of inertia prefactor  $f = 0.3307$  is smaller than the value 0.4 for a homogeneous sphere (see problem 2), another indication of mass concentration towards the earth's centre.

**problem: 1** Derive the following expression for the moment of inertia of a spherically symmetric Earth model with outer radius  $R$ ,

$$I = \frac{8\pi}{3} \int_0^R \rho(r)r^4 dr \quad (3)$$

*Hint: use the symmetry and compute  $I = \frac{1}{3}(I_x + I_y + I_z)$ , where  $I_x$  is the moment of inertia with respect to a rotation axis coinciding with the  $x$ -axis.*

**problem: 2** Derive from (3) the value of the prefactor  $f$  of the moment of inertia for a uniform sphere. answer:  $f = 2/5$ .

*In general the moment of inertia prefactor  $f$  is an indicator of the degree of mass concentration towards the centre of a spherically symmetric mass distribution. Endmembers of mass concentration are a) a concentrated central point mass and b) all mass concentrated on a spherical surface of zero thickness.*

*Verify that the moment of inertia of the point mass endmember equals zero and that for the prefactor for a spherical shell of vanishing thickness we have  $f = \frac{2}{3}$ .*

Wiechert's two-layer model with a distinct core is constrained by the moment of inertia prefactor  $f$ , the mantle radius  $R$  and density  $\rho_m$  and the total mass  $M$  or, equivalently, the mean density  $\langle \rho \rangle$ . Expressions for the core radius  $R_c$  and density  $\rho_c$  can be formulated for this model as specified in the following exercise (Bullen, 1975).

**problem: 3** Derive a 2-parameter model for the earth's 1-D radial density distribution  $\rho(r)$  consisting of two uniform layers (core and mantle) of radius  $R_c$  and  $R$  respectively and with contrasting uniform densities  $\rho_c$  and  $\rho_m$  for core and mantle respectively. Assume  $\rho_m$  to be known, leaving  $\rho_c$  and  $R_c$  as unknown parameters that can be determined from the known moment of inertia prefactor  $f$  and the average density  $\langle \rho \rangle$ .

*Derive the following expressions for  $R_c$  and  $\rho_c$ ,*

$$\frac{R_c}{R} = \left( \frac{\frac{5}{2}f \frac{\langle \rho \rangle}{\rho_m} - 1}{\frac{\langle \rho \rangle}{\rho_m} - 1} \right)^{1/2}, \quad \rho_c = \rho_m \left\{ 1 + \left( \frac{R}{R_c} \right)^3 \left( \frac{\langle \rho \rangle}{\rho_m} - 1 \right) \right\} \quad (4)$$

*Hint: First derive the following expressions,*

$$\langle \rho \rangle = \frac{3}{R^3} \int_0^R \rho r^2 dr, \quad fR^5 \langle \rho \rangle = 2 \int_0^R \rho r^4 dr \quad (5)$$

In Bullen's two-layer model the core radius is assumed to be known from seismology. For this model the mantle and core densities can be expressed in the known parameters in the following problem.

**problem: 4** Assume the core radius  $R_c$  to be a known parameter in the following. Derive a 2-parameter model for the earth's 1-D radial density distribution  $\rho(r)$  consisting of two uniform layers (core and mantle), with a core and mantle radius  $R_c$  and  $R$  and different uniform densities  $\rho_m$  and  $\rho_c$  for mantle and core. Express the parameters  $\rho_m$  and  $\rho_c$  in terms of the mass and moment of inertia.

*Solution: in matrix-vector format,*

$$\begin{pmatrix} \rho_c \\ \rho_m \end{pmatrix} = \frac{4\pi}{3\Delta} \begin{pmatrix} \frac{2}{5}(R^5 - R_c^5) & -(R^3 - R_c^3) \\ -\frac{2}{5}R_c^5 & R_c^3 \end{pmatrix} \begin{pmatrix} M \\ I \end{pmatrix} \quad (6)$$

where the determinant  $\Delta = \frac{32\pi^2}{45} (R_c^3(R^5 - R_c^5) - R_c^5(R^3 - R_c^3))$ .

**problem: 5** The numerical value of the interim expressions in (6) exceeds the magnitude of single precision real type variables in computer programs, that are limited to approximately  $1.7 \cdot 10^{38}$ . A work around for this problem may be to use double precision real variables that have a higher maximum magnitude of about  $10^{308}$ .

An alternative solution is to switch to using non-dimensional parameters, denoted by primes, in the following way: define  $R'_c = R_c/R$ ,  $M = 4/3 \cdot \pi R^3 \langle \rho \rangle$  and  $M' = 1$ .  $\rho_c = \langle \rho \rangle \rho'_c$ ,  $\rho_m = \langle \rho \rangle \rho'_m$  and express the moment of inertia in the mean density and outer radius as,  $I = fMR^2 = 4/3 \cdot \pi R^5 \langle \rho \rangle f$ . With these definitions rewrite (6) into the non-dimensional form,

$$\begin{pmatrix} \rho'_c \\ \rho'_m \end{pmatrix} = \frac{16\pi^2}{9\Delta'} \begin{pmatrix} \frac{2}{5}(1 - R_c'^5) & -(1 - R_c'^3) \\ -\frac{2}{5}R_c'^5 & R_c'^3 \end{pmatrix} \begin{pmatrix} M' \\ f \end{pmatrix} \quad (7)$$

where the determinant  $\Delta' = \frac{32\pi^2}{45} (R_c'^3(1 - R_c'^5) - R_c'^5(1 - R_c'^3))$ .

## 2.3 Density, gravity and pressure in the Earth

In the Earth's mantle major solid state phase transitions occur in the silicate material which constitutes the planetary mantle outside the metallic iron/nickel core. These phase transitions are induced by the increase in the static pressure from a 1 bar ( $10^5$  Pa) atmospheric value at the Earth's surface to  $136 \cdot 10^9$  Pa at the core mantle boundary at a depth of approximately 2900 km. Phase transitions in the Earth's interior are associated with changes in the elastic wave velocities that can be deduced from seismological observations. In high pressure experiments, phase transitions in candidate mantle silicates can be studied and correlated with the seismological data to constrain the mineralogy and pressure/temperature distribution in the mantle. Knowledge of the internal material constitution of the Earth, such as the mineral phase, is a requirement for understanding the main geodynamical processes that determine Earth's evolution.

Density and pressure inside the Earth are linked with self-gravitation. This means that the hydrostatic or lithostatic pressure is a direct result of the gravity field generated by the Earth's own mass distribution. The lithostatic pressure can be expressed as the weight of a column of unit cross-sectional area extending from zero depth, at the Earth's surface, to the depth  $z$  of the evaluation point,

$$P(z) = \int_0^z \rho(z')g(z')dz' \quad (8)$$

where  $\rho$  is the mass density and  $g$  is the magnitude of the gravitational acceleration.

The gravity field defining  $g$  is generated by the Earth's own density distribution. Weak periodic gravity 'perturbations' are generated by celestial bodies, expressed in the external tides, both ocean tides and solid earth tides. The main tides are generated by the Earth's moon and by the Sun.

In the following section expressions for the gravity field in terms of the density distribution are given, based on Newtons law of gravitation.

In the description of the density distribution we will first neglect the role of self-compression and consider a number of one-dimensional (1-D), spherically symmetric, parameterized density distributions. Self-compression and compressibility are then treated in section 2.6. Self-compression and finite compressibility result in a continuous increase of density with pressure in agreement with several geophysical observations.

**problem: 6** Derive the expression (8) (where the depth  $z$  is not to be confused with a cartesian coordinate) for the lithostatic pressure in a spherically symmetric planet from the elastostatic equation for a static medium,

$$\partial_j \sigma_{ij} + \rho g_i = 0 \quad (9)$$

*Hint: Assume hydrostatic conditions where the stress tensor can be written as  $\sigma_{ij} = -P\delta_{ij}$ , with  $\delta_{ij}$  the Kronecker delta, and derive from equation (9) for the pressure gradient,  $\nabla P = \rho \mathbf{g}$ .*

## 2.4 Gravity field of a mass distribution

Newton formulated the attraction force acting on a point mass  $m_0$ , located in a point with position vector  $\mathbf{r} = (x, y, z)$ , with  $x, y, z$  the cartesian coordinates, from a second point mass  $m_1$  located at  $\mathbf{r}_1 = (x_1, y_1, z_1)$ , illustrated in Fig. 2 as,

$$\mathbf{F}(\mathbf{r}) = \frac{Gm_0m_1}{|\mathbf{r}_1 - \mathbf{r}|^2} \mathbf{e}_{\mathbf{r}\mathbf{r}_1} \quad (10)$$

Where  $\mathbf{e}_{\mathbf{r}\mathbf{r}_1}$  is the unit vector in  $\mathbf{r}$  pointing towards  $\mathbf{r}_1$  and  $\mathbf{F}(\mathbf{r}_1) = -\mathbf{F}(\mathbf{r})$ .  $\mathbf{r}, \mathbf{r}_1$  are the position vectors of the two point masses and  $|\mathbf{r}_1 - \mathbf{r}| = \sqrt{(x_1 - x)^2 + (y_1 - y)^2 + (z_1 - z)^2}$  is the distance between the points  $\mathbf{r}$  and  $\mathbf{r}_1$ .  $G$  is the gravitational constant  $G = 6.6732 \times 10^{-11} \text{ Nm}^2\text{kg}^{-2}$ ,  $m_0, m_1$  the mass of the respective pointmasses.

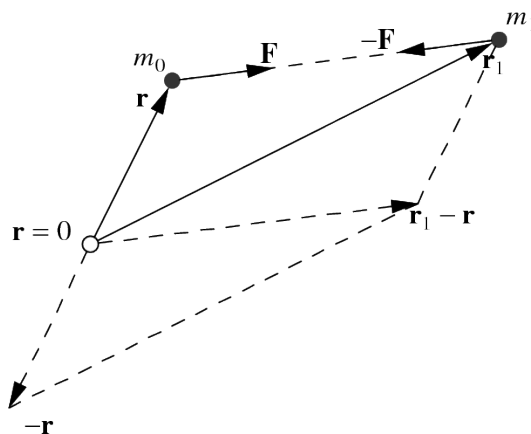


Figure 2: Vector diagram of the gravitational forces acting on the two point masses  $m_0, m_1$  in vector locations  $\mathbf{r}$  and  $\mathbf{r}_1$  respectively. From the expression for the gravity field (10) it follows that the forces on both masses are of equal magnitude and in opposite direction.

This gravitation effect is usually specified as a gravitation force per unit mass or acceleration vector  $\mathbf{g}$ ,

$$\mathbf{g}(\mathbf{r}) = \frac{Gm_1}{|\mathbf{r}_1 - \mathbf{r}|^2} \mathbf{e}_{\mathbf{r}\mathbf{r}_1} \quad (11)$$

It can be verified by inspection that the acceleration vector field can be written as the gradient of a scalar potential field  $U(\mathbf{r})$  with  $\mathbf{g} = -\nabla U = (-\frac{\partial U}{\partial x}, -\frac{\partial U}{\partial y}, -\frac{\partial U}{\partial z})$ , (see problem 10),

$$U(\mathbf{r}) = -\frac{Gm_1}{|\mathbf{r}_1 - \mathbf{r}|} \quad (12)$$

The gravity acceleration and corresponding potential field are additive such that the total force or potential of a collection of point masses is obtained by summation over individual point contributions,

$$\mathbf{g}(\mathbf{r}) = \sum_j \frac{Gm_j}{|\mathbf{r}_j - \mathbf{r}|^2} \mathbf{e}_{\mathbf{r}\mathbf{r}_j}, \quad U(\mathbf{r}) = -\sum_j \frac{Gm_j}{|\mathbf{r}_j - \mathbf{r}|} \quad (13)$$

With this definition and sign convention the potential field of a point source in the origin is represented by a potential well ( $U(\mathbf{r}) < 0$ ). This is known as Coulomb's law and the equivalent form for a continuous mass distribution of density  $\rho$  (mass per unit volume) contained in a volume  $V$  is,

$$\mathbf{g}(\mathbf{r}) = \int_V \frac{G\rho(\mathbf{r}')}{|\mathbf{r}' - \mathbf{r}|^2} \mathbf{e}_{\mathbf{r}\mathbf{r}'} dV(\mathbf{r}'), \quad U(\mathbf{r}) = -\int_V \frac{G\rho(\mathbf{r}')}{|\mathbf{r}' - \mathbf{r}|} dV(\mathbf{r}') \quad (14)$$

Besides the integral expression for the gravity field defined in (14) there is also the differential form using the second order partial differential equations of Laplace and Poisson. It can be shown by verification that  $U$  in (14) satisfies Poisson's equation,

$$\nabla^2 U = 4\pi G\rho \quad (15)$$

which reduces to Laplace's equation  $\nabla^2 U = 0$  outside the mass distribution in  $V$  (where  $\rho = 0$ ).<sup>4</sup>

In Newton's time the numerical value of  $G$  had not been determined yet. As a result it was not possible to determine the mass of the Earth  $M_\oplus$  by measuring the gravitation force of the Earth on a known 'test mass'. This way only the value of  $GM_\oplus$  could be determined. Only with the experiment named after Cavendish (1798)<sup>5</sup> it became possible to measure  $G$  directly, in a torsion balance experiment, by determining the gravitational attraction of two closely spaced test masses.

<sup>4</sup>To show that  $U$  in (14) satisfies Poisson's equation integrate the normal component of the acceleration field over an arbitrary closed surface  $S$  enclosing  $V$  and change the order of integration for the volume and surface integral.

$$\int_S \nabla U(\mathbf{r}) \cdot \mathbf{n} dA(\mathbf{r}) = -\int_V G\rho(\mathbf{r}') \left\{ \int_S \nabla \left( \frac{1}{|\mathbf{r}' - \mathbf{r}|} \right) \cdot \mathbf{n} dA(\mathbf{r}) \right\} dV(\mathbf{r}') \quad (16)$$

The surface integral on the right is independent of the choice of the surface  $S$  as long as it contains  $\mathbf{r}'$ . We therefore replace this surface by a sphere of radius  $R$  centered at  $\mathbf{r}'$  and find for the surface integral the value  $-4\pi$ . Next we apply the Gauss divergence theorem to the left hand surface integral to obtain,

$$\int_V \nabla^2 U dV = \int_V 4\pi G\rho dV \quad (17)$$

Note that the surface has been contracted on the volume  $V$  to obtain (17). Since the surface and enclosed volume are arbitrary we obtain the Poisson equation,

$$\nabla^2 U = 4\pi G\rho \quad (18)$$

<sup>5</sup>[http://en.wikipedia.org/wiki/Cavendish\\_experiment](http://en.wikipedia.org/wiki/Cavendish_experiment)

### 2.4.1 Problem section: spherically symmetric density distributions and corresponding gravity fields

**problem: 7** Verify that the familiar surface value of the Earth's gravity acceleration  $g_0 = 9.8 \text{ m/s}^2$  corresponds to the value of a point mass at the Earth's centre with the same mass as the Earth, (see Table 1).

**problem: 8** Compute the Earth's mass  $M_\oplus$  from the given values of the gravity acceleration at the surface  $g_0$ , the gravitational constant  $G$  and the planet radius.

**problem: 9** Fig. 1 suggests that the magnitude of the gravity acceleration is approximately constant throughout the Earth's mantle. Therefore assume an approximate uniform value of  $g$  in the Earth's mantle,  $g_m \sim 10 \text{ m/s}^2$  and use an approximate average mantle density  $\rho_m \sim 4.5 \cdot 10^3 \text{ kg/m}^3$  (see Fig. 1) to obtain from (8) an approximation of the static pressure at the approximate depth of the core mantle boundary 3000 km.

**problem: 10** Verify the consistency of the expression for the gravity acceleration and potential of a point mass in (11) and (12), i.e. proof from these expressions by explicit calculation of the gradient vector from the scalar potential field that  $\mathbf{g} = -\nabla U$ .

*Hint: specify the potential in cartesian coordinates and differentiate the result with respect to the coordinates  $x, y, z$ .*

**problem: 11** Apply the Poisson equation (15) to obtain the gravity field of a point-mass distribution with mass  $M$ , described by a Dirac delta function,  $\rho(\mathbf{r}) = M\delta(\mathbf{r} - \mathbf{r}_0)$ . Where the following property holds for the delta function,

$$\int_V \delta(\mathbf{r} - \mathbf{r}_0) dV = \begin{cases} 1, & \mathbf{r}_0 \in V \\ 0, & \mathbf{r}_0 \notin V \end{cases} \quad \text{or, more general} \quad \int_V f(\mathbf{r})\delta(\mathbf{r} - \mathbf{r}_0) dV = \begin{cases} f(\mathbf{r}_0), & \mathbf{r}_0 \in V \\ 0, & \mathbf{r}_0 \notin V \end{cases} \quad (19)$$

*Hint: integrate (15) over a spherical volume, centered at  $\mathbf{r}_0$  and apply the Gauss divergence theorem: for a vector field  $\mathbf{A} = (A_1, A_2, A_3)$  with divergence  $\nabla \cdot \mathbf{A} = \frac{\partial A_1}{\partial x} + \frac{\partial A_2}{\partial y} + \frac{\partial A_3}{\partial z}$*

$$\int_V \nabla \cdot \mathbf{A} dV = \int_{\partial V} \mathbf{A} \cdot \mathbf{n} dS \quad (20)$$

where  $\partial V$  is the closed boundary surface of  $V$ .

**problem: 12** Check the dimensional units in (15) and verify that the gravitational potential has the dimension of energy per unit mass. This is in agreement with the identification of the gravity potential with the potential (gravitational) energy of a unit mass in the gravity field. <sup>6</sup>

<sup>6</sup>The local potential field value  $U(\mathbf{r}_1)$  equals the negative of the (gravitational) potential energy  $W(\mathbf{r}_1)$  of a unit point mass positioned at  $\mathbf{r}_1$ . It can be shown that the change in potential energy  $\Delta W$  that results from moving a unit mass from  $\mathbf{r}_1$  to  $\mathbf{r}_2$  follows directly from the potential field values  $U(\mathbf{r}_1)$ ,  $U(\mathbf{r}_2)$  and is independent of the path taken between  $\mathbf{r}_1$  and  $\mathbf{r}_2$ . This property defines a so called conservative field  $U$ .

To derive this result we compute the potential energy difference as the path (line) integral of the work done by the gravity force field on a unit mass and apply the gradient property  $\mathbf{g} = -\nabla U$ . The work done by moving a unit point mass from a location  $\mathbf{r}_1$  to  $\mathbf{r}_2$  is defined by the line integral,

$$\Delta W = \int_{\mathbf{r}_1}^{\mathbf{r}_2} \mathbf{F} \cdot d\mathbf{r} = \int_{\mathbf{r}_1}^{\mathbf{r}_2} \mathbf{g} \cdot d\mathbf{r} = \int_{\mathbf{r}_1}^{\mathbf{r}_2} -\nabla U \cdot d\mathbf{r} = \int_{U(\mathbf{r}_1)}^{U(\mathbf{r}_2)} -dU = -(U(\mathbf{r}_2) - U(\mathbf{r}_1)) = -\Delta U \quad (21)$$

Here the following gradient property has been used, relating the gradient vector to the differential of the scalar potential

The above can be applied in the determination of the escape velocity from the surface of a planet. This is the minimum launch velocity to escape from the planet's gravity field. For a spherically symmetric planet the external gravity potential is given by (30). Moving an object from the surface, the gravity potential changes by  $\Delta U = U(r) - U(R) = GM(-\frac{1}{r} + \frac{1}{R})$ . Applying an energy conservation argument we require the change in total (potential plus kinetic) energy per unit mass to be:  $\Delta E = \Delta U + \Delta K = 0$ . With  $\Delta K = -v_{ex}^2/2$  we get  $v_{esc} = \sqrt{2GM/R}$ .

**problem: 13** Compute the surface escape velocities for different celestial bodies using the parameters given in Table 1

	Radius km	Mass kg	Density kg/m <sup>3</sup>
Earth	6371	$5.97 \cdot 10^{24}$	$5.515 \times 10^3$
Moon	1738	$7.34 \cdot 10^{22}$	$3.34 \times 10^3$
Mars	3394	$6.42 \cdot 10^{23}$	$3.93 \times 10^3$
Jupiter	71492	$1.9 \cdot 10^{27}$	$1.326 \times 10^3$
Sun	$6.96 \cdot 10^5$	$1.99 \cdot 10^{30}$	-

Table 1: Radius-mass parameters of Earth moon and planets.

**problem: 14** The potential energy of a self-gravitating planet in its own gravity field is defined in terms of the volume density  $\rho U$  as,

$$E = - \int_V \rho U dV \quad (24)$$

Derive the following expression for the potential energy of a spherically symmetric, uniform density model, using the expression for the internal gravity potential defined in (29)

$$E = \frac{8\pi}{5} G \rho_0 M R^2 \quad (25)$$

Compute the potential energy value  $E$ , assuming a density  $\rho_0 = 5.5 \cdot 10^3 \text{kg/m}^3$  and planetary radius  $R = 6371 \text{km}$ .

answer:  $4.4 \cdot 10^{32} \text{J}$

The gravitational energy considered above plays an important role in major compositional differentiation processes that occurred in the early Earth and are still occurring today.

field,

$$dU = \frac{\partial U}{\partial x} dx + \frac{\partial U}{\partial y} dy + \frac{\partial U}{\partial z} dz = \nabla U \cdot d\mathbf{r} \quad (22)$$

The gravitational potential field can thus be defined in terms of the work done by the gravity field to move a unit mass from infinity to the evaluation point.

$$W(\mathbf{r}_1) = \int_{\mathbf{r}_\infty}^{\mathbf{r}_1} \mathbf{g} \cdot d\mathbf{r} = \int_{\mathbf{r}_\infty}^{\mathbf{r}_1} -\nabla U \cdot d\mathbf{r} = \int_{U(\mathbf{r}_\infty)}^{U(\mathbf{r}_1)} -dU = -U(\mathbf{r}_1) + U(\mathbf{r}_\infty) = -U(\mathbf{r}_1) \quad (23)$$

Where  $U(\mathbf{r}_\infty) = 0$  has been used.

- A so called ‘core catastrophe’ occurred when the iron/nickel core of the Earth differentiated from the silicate mantle in the first few million years after the formation of the Earth in the early solar system. This event has probably freed enough potential energy to melt the mantle completely, resulting in a global magma ocean.
- Crystallization of the solid inner core from the liquid outer core, as a result of core cooling, is accompanied by compositional differentiation. The liquid outer core contains a lighter fraction, possibly sulfur, which stays behind in the liquid during freezing of the inner core. The enriched residual liquid near the inner core boundary is less dense than the average liquid of the outer core and this results in a gravitationally unstable layering that induces ‘chemically driven’ convective flow in the outer core. The potential energy released in this chemical convection is probably an important energy source in powering the geodynamo that generates the Earth’s present day magnetic field.

## 2.5 The gravity and pressure field for parameterized density models with self-gravitation

In the following problems a number of simple density distributions are investigated that will serve as a reference for models more constrained by geophysical observations to be introduced in later sections. The gravity field can be determined by solving the governing Poisson equation (15) using suitable boundary conditions. For the special case of spherically symmetric mass distributions simple 1-D integral expressions can be used to derive the corresponding radial pressure distribution.

**problem: 15** *The internal and external gravity field for a simple model of a planet can be derived by solving the Poisson equation (15), and applying appropriate boundary conditions to the general solution. Consider a spherically symmetric planet of radius  $R$  and uniform density  $\rho_0$ .*

1. *Derive expressions for the gravity potential field  $U$  and the gravity force field  $g = |\mathbf{g}|$  inside and outside the planet.*

*Hints: Solve Poisson’s equation in spherical coordinates for the interior ( $r \leq R$ ) and exterior domain  $r \geq R$  separately. The separate solutions for the interior  $U_{int}, g_{int}$  and exterior  $U_{ext}, g_{ext}$  domain each contain two integration constants which can be determined by applying the following boundary conditions,*

$$\lim_{r \rightarrow \infty} U_{ext}(r) = 0, \quad \lim_{r \rightarrow 0} g_{int}(r) < \infty \quad (26)$$

*Continuity of the gravity acceleration  $g$  at the surface  $r = R$ ,*

$$g_{int}(R) = g_{ext}(R) \quad (27)$$

*Continuity of the gravity potential  $U$  at the surface  $r = R$ ,*

$$U_{int}(R) = U_{ext}(R) \quad (28)$$

*Answers*

$$g_{int} = \frac{4\pi}{3}G\rho_0 r, \quad U_{int} = \frac{2\pi}{3}G\rho_0 r^2 - \frac{3}{2} \frac{GM}{R} \quad (29)$$

*where  $M = \frac{4\pi}{3}R^3\rho_0$  is the planet mass and  $G$  is the gravitational constant.*

$$g_{ext} = \frac{GM}{r^2}, \quad U_{ext} = -\frac{GM}{r} \quad (30)$$

2. Verify that the external gravity force field is identical to the field of a concentrated point mass at  $r = 0$ . Derive a corresponding relation between the internal gravity force field and a (different) concentrated point mass,  $m(r)$  at the center (see also (31)).
3. Derive an expression for the radial distribution of the pressure in the planetary interior and compute the central pressure for a case with  $\rho_0 = 5.5 \cdot 10^3 \text{ kg m}^{-3}$  and  $R = 6.371 \times 10^6 \text{ m}$ .

Solution:  $P(r) = \frac{2\pi}{3} \rho_0^2 G (R^2 - r^2)$

The gravity field of a spherically symmetric density distribution is identical to the field of an equivalent point-mass.<sup>7</sup> This can be formulated as follows,

$$g(r) = \frac{Gm(r)}{r^2}, \quad m(r) = \int_{V(r)} \rho dV = \int_0^r \rho(r') 4\pi r'^2 dr' \quad (31)$$

Here  $m(r)$  is the mass inside a sphere of radius  $r$  and  $g(r)$  is the corresponding magnitude of the gravity acceleration. For the corresponding gravity potential this implies, with  $\int_r^\infty \frac{dU}{dr'} dr' = U(\infty) - U(r) = -U(r)$ ,

$$U(r) = - \int_r^\infty \frac{dU}{dr'} dr' = \int_r^\infty g_r(r') dr' = \int_r^\infty -g(r') dr' = - \int_r^\infty \frac{Gm(r')}{r'^2} dr' \quad (32)$$

where the radial vector component  $g_r$  has been expressed in the vector length  $g$  as  $g_r = \mathbf{g} \cdot \mathbf{e}_r = -g$ .

To derive (31), the potential field at the radial coordinate  $r$  can be split in contributions originating from an internal- and external density distribution  $U(r) = U_i(r) + U_e(r)$ . With corresponding pairs,  $U_i \leftrightarrow \rho_i$ , and  $U_e \leftrightarrow \rho_e$ , where  $\rho_e(r') = 0$ ,  $r' \leq r$ , and  $\rho_e(r') = \rho(r')$ ,  $r' > r$ . This follows from the linearity of the governing Poisson equation.

The field generated by the internal mass distribution is obtained by integrating the corresponding Poisson equation in spherical coordinates,

$$\frac{1}{r'^2} \frac{d}{dr'} r'^2 \frac{dU_i}{dr'} = 4\pi G \rho_i \quad (33)$$

$$\int_0^r \frac{d}{dr'} \left( r'^2 \frac{dU_i}{dr'} \right) dr' = \int_0^r 4\pi G \rho_i r'^2 dr' \quad (34)$$

The radial component of the gravity acceleration becomes,

$$g_r(r) = - \frac{dU_i}{dr} = - \frac{1}{r^2} \int_0^r 4\pi G \rho_i r'^2 dr' = - \frac{Gm(r)}{r^2} \quad (35)$$

Furthermore the acceleration field  $g_e$  from the external mass distribution  $\rho_e$  for internal evaluation points  $r' < r$  is zero. The corresponding gravity potential  $U_e$  is uniform, which follows from the relevant Poisson equation, in spherical coordinates for a spherically symmetric mass distribution,

$$\frac{1}{r'^2} \frac{d}{dr'} r'^2 \frac{dU_e}{dr'} = 4\pi G \rho_e = 0 \rightarrow r'^2 \frac{dU_e}{dr'} = A \rightarrow g_e(r') = - \frac{dU_e}{dr'} = - \frac{A}{r'^2} \quad (36)$$

A non-singular field requires  $A = 0$ ,  $g_e(r') = 0$ ,  $r' \leq r$  and,

$$\frac{dU_e}{dr'} = 0 \rightarrow U_e(r') = B, \quad r' \leq r \quad (37)$$

---

<sup>7</sup>See problem 15 for the special case of a uniform density distribution.

**problem: 16** Verify that (31) and (32), applied to the special case of a homogeneous sphere of density  $\rho_0$ , lead to the same expression for the internal and external potential and acceleration field as given in problem 15.

For a two-parameter spherically symmetric planet model consisting of a uniform core and mantle with radius  $R_c$  and  $R_m$  and contrasting densities  $\rho_c$  and  $\rho_m$ , the gravity field can also be determined by solving the Poisson equation for the particular density distribution and determination of the integration constants from the boundary conditions. However in this case the formula (31) are more convenient to obtain expressions for the gravity field.

**problem: 17** Derive expressions for the gravity acceleration and internal pressure distribution for the two-parameter model

$$\rho(r) = \begin{cases} \rho_c, & r < R_c \\ \rho_m, & R_c < r \leq R \\ \rho_e = 0, & r > R \end{cases}, \quad g(r) = \begin{cases} g_c, & r < R_c \\ g_m, & R_c < r \leq R \\ g_e, & r > R \end{cases}, \quad P(r) = \begin{cases} P_c, & r < R_c \\ P_m, & r \geq R_c \end{cases} \quad (38)$$

using (31) and (8). See also (44).

**Answer:**

$$g_c(r) = \frac{4\pi}{3}G\rho_c r, \quad g_m(r) = \frac{G}{r^2} \left\{ \frac{4\pi}{3}\rho_m (r^3 - R_c^3) + M_c \right\}, \quad g_e(r) = \frac{G}{r^2} (M_m + M_c) \quad (39)$$

$$M_c = \frac{4\pi}{3}R_c^3\rho_c, \quad M_m = \frac{4\pi}{3}\rho_m (R^3 - R_c^3) \quad (40)$$

$$P_c(r) = P_m(R_c) + \frac{2\pi}{3}G\rho_c^2 (R_c^2 - r^2) \quad (41)$$

$$P_m(r) = \frac{2\pi}{3}G\rho_m^2 \left\{ R_m^2 - r^2 + 2 \left( \frac{\rho_c}{\rho_m} - 1 \right) R_c^3 \left( \frac{1}{r} - \frac{1}{R_m} \right) \right\} \quad (42)$$

## 2.6 The pressure effect on density

### 2.6.1 Introduction

In the previous sections we considered the gravity field of a given mass distribution. For self-gravitating planets of sufficient size the local density depends on the pressure, through self-compression i.e. the compression of the material caused by the planets own gravity field. As we have seen in previous sections the lithostatic pressure depends on the gravity field and the density distribution. It follows that the determination of the density, gravity and pressure are coupled problems that must be solved simultaneously and can not be solved separately. Here we will consider the solution of such coupled problems.

From observations of the average density of surface rocks of some  $2.7 \cdot 10^3 \text{ kg/m}^3$  and the known mean density of the Earth  $5.5 \cdot 10^3 \text{ kg/m}^3$ , it follows that the surface density is less than halve the mean Earth value. The difference between both density values suggests a density increase in the interior which could be related either to different composition at depth, for example corresponding to a dense metallic core, and/or the effect of self-compression in an otherwise homogeneous planet. Solid state phase transitions of mantle material due to increasing pressure can also explain part of the high mean density value.

From the nineteenth century on, models of the internal density distribution of the earth have been investigated. These models have in common that the radial density distribution is parameterized in a simple way with a small number of parameters, typically two, which are then adjusted to the known data such as the surface density and the Earth's total mass or moment of inertia.

In the following the relation between density, gravity and pressure in a self-gravitating planet will be investigated in a more self consistent way.

For a spherically symmetric density distribution the corresponding magnitude of the gravity acceleration vector is given by (35),

$$g(r) = |g_r(r)| = \frac{4\pi G}{r^2} \int_0^r \rho(r') r'^2 dr' = \frac{Gm(r)}{r^2} \quad (43)$$

where  $m(r)$  is the mass of a sphere of radius  $r$  and  $\rho(r)$  is the corresponding radial density profile.

**problem: 18** Use (43) to show that it is not possible to derive a unique radial mass distribution of a spherically symmetric planet from the observed surface value of the gravity field alone. This can be verified by showing that multiple density profiles exist that produce the same surface gravity. To illustrate this sketch a schematic internal radial profile of the gravity acceleration in a comparison of two spherically symmetric planets of identical mass  $M$  and radius  $R$ . The first one is a homogeneous planet with density  $\rho_0$  and the second one is a differentiated planet with a uniform high density core  $\rho_c = \rho_0 + \delta\rho$  and less dense mantle  $\rho_m = \rho_0 - \delta\rho$ . Verify that these assumptions correspond to this special case with volume fraction of the core  $\phi_c = 1/2$ .

The same external gravity field is obtained with a spherical shell of zero thickness and radius  $r$ , with a uniform surface mass density  $\sigma(r) = M/(4\pi r^2)$ , (a uniform mass sheet) as a special case of (31). It can be shown more generally that for the external gravity field of a non-spherically symmetric mass distribution, equivalent non-uniform mass sheets can be defined generating the same external gravity field.

From the above results the lithostatic pressure distribution can be obtained by substitution for the

gravity acceleration and integrating the pressure gradient  $dP/dr = -\rho g$ . Assuming a zero pressure value at the surface this results in,

$$P(r) = \int_r^R \rho(r')g(r')dr' = 4\pi G \int_r^R \rho(r') \left\{ \frac{1}{r'^2} \int_0^{r'} \rho(r'')r''^2 dr'' \right\} dr' \quad (44)$$

The pressure in the Earth's interior reaches values over 350 GPa as shown in Fig. 1. For such high pressure values the effect of self-compression on the density is significant. In the following this effect is further explored.

The incompressibility  $K$ , or bulkmodulus <sup>8</sup>, is defined as,

$$\frac{1}{K} = \frac{1}{\rho} \frac{d\rho}{dP} \quad (45)$$

By substitution of  $dP = -\rho g dr$  in (45) we derive a differential equation for the density profile of a compressible planet model,

$$\frac{1}{K} = \frac{-1}{\rho^2 g} \frac{d\rho}{dr} \Rightarrow \frac{d\rho}{dr} = -\frac{\rho^2 g}{K} \quad (46)$$

### 2.6.2 Parameterization of the bulkmodulus

The radial density distribution for a selfcompressing planet can be obtained from (46) once the bulkmodulus  $K$  is known. We will first consider simple cases where  $K$  is either a uniform constant or it is parameterized in terms of the density.

**problem: 19** Assume both  $K$  and  $g$  in (46) to be uniform in the mantle and derive the following density profile, <sup>9</sup>

$$\rho(z) = \frac{\rho_0}{1 - \frac{\rho_0 g z}{K}} \quad (51)$$

where  $z = R - r$  is the depth coordinate and  $\rho_0 = \rho(0)$  is the surface density value.

<sup>8</sup>An isotropic linear elastic solid can be described by two independent elasticity parameters, for instance the Lamé parameters  $\lambda$  and  $\mu$ . The bulkmodulus can be expressed in the Lamé parameters as,  $K = \lambda + \frac{2}{3}\mu$ . The bulkmodulus  $K$  and the shearmodulus  $\mu$  are the most commonly used parameters to specify the elastic parameters of Earth materials.

<sup>9</sup>Hint: First order ordinary differential equations like (46) are of so called separable form,

$$\frac{dy}{dx} = P(y)Q(x) \quad (47)$$

(see for instance, E.L. Ince, *Integration of ordinary differential equations*, Oliver and Boyd, 1956) in which case they can be integrated in the following way,

$$\frac{dy}{P(y)} = Q(x)dx \rightarrow \int \frac{dy}{P(y)} = \int Q(x)dx + C \rightarrow \quad (48)$$

In cases where the lefthand integral is a known function, say  $f(y)$ , the solution is obtained by the inverse function,

$$y(x) = f^{-1} \left( \int Q(x)dx + C \right) \quad (49)$$

Example:  $dy/dx = -y^2 e^{-x}$ ,  $x \geq 0$ ,

$$\int -\frac{dy}{y^2} = \int e^{-x} dx + C \rightarrow \frac{1}{y} = -e^{-x} + C \rightarrow y(x) = \frac{1}{C - e^{-x}} \quad (50)$$

The integration constant  $C$  can be expressed in an initial condition,  $C = 1 + 1/y(0)$ .

- Compute the depth  $z_1$  where the expression (51) becomes singular, i.e.  $\rho \rightarrow \infty$ , suggesting infinite compression of the material. To do this assume Earth(mantle)-like values of the incompressibility,  $K = 400\text{GPa}$  (see Fig.3) and the surface density  $\rho_0 = 3 \cdot 10^3 \text{ kg/m}^3$ .
- Now consider a simplified model of a large rocky exoplanet of Earth-like composition with  $M = 8M_\oplus$  and  $R = 1.5R_\oplus$ . Assume uniform gravity (adapted for the given  $M, R$ ) and uniform incompressibility  $K$ . Do you now find the singular depth  $z_1$  within the depth range of the planet? Comment on the assumption of a uniform gravity field in view of the models presented in section 2.5.

**problem: 20** The result of problem 19 gives the density depth distribution for the model with constant properties. The resulting expression (51) also contains the uniform gravity acceleration. A more fundamental relation between density and pressure, not including gravity, can be derived for this model with constant material property  $K$  as an equation of state (EOS) for the density.

Derive from the definition of the bulkmodulus (45) the following logarithmic EOS for the density in terms of the static pressure,

$$P = \ln \left( \left( \frac{\rho}{\rho_0} \right)^K \right) \quad (52)$$

The EOS (52) can be inverted to obtain an explicit expression for density as a function of pressure,

$$\rho(P) = \rho_0 \exp \left( \frac{P}{K} \right) \quad (53)$$

The singular behavior in the density model of problem 19 is a result of the assumed uniform  $g$  and  $K$  in (46). While  $g$  is reasonably constant with depth in the mantle, as illustrated in Fig. 1,  $K$  is not. The incompressibility increases with increasing depth/pressure and as a result the compression remains finite for earth-like conditions. The incompressibility can be expressed in the density and the seismic wave velocities,  $v_p = \sqrt{(\lambda + 2\mu)/\rho}$ ,  $v_s = \sqrt{\mu/\rho}$ . With  $K = \lambda + \frac{2}{3}\mu$  this becomes  $K = \rho(v_p^2 - 4/3v_s^2)$ . A radial profile  $K(P(r))$  can therefore be derived, from the seismic velocities determined from inversion of traveltime tables of longitudinal and shearwave seismic arrivals.

The  $K(P(r))$  profile derived from the PREM model of Dziewonski and Anderson (1981) appears to be roughly linear as shown in Fig.3.

A linear relation between bulkmodulus and pressure as suggested by Fig. 3, is also obtained using the following power law parameterization for the bulkmodulus in terms of the density  $K(\rho)$ .

$$K = C\rho^n \Rightarrow \ln(K) = \ln(C) + n \ln(\rho) \Rightarrow n = \frac{d \ln(K)}{d \ln(\rho)} = \frac{dK}{dP} = K'_0 \quad (54)$$

where  $C$  is a constant. The constant pressure derivative in this model implies a linear pressure relation  $K(P) = K_0 + K'_0 P$ . This appears to approximate the distribution of  $K$  in particular in the lower mantle as determined from seismological data in the PREM model.  $K'_0 \approx 4$  for the magnesium-iron silicates (Mg, Fe)SiO<sub>3</sub> (perovskite) and dense oxides (Mg, Fe)O (wüstite), representative for the earth's deep mantle. <sup>10</sup>

<sup>10</sup>An equation of state directly relating the density or specific volume,  $V = 1/\rho$ , to pressure can be derived from such an 'ansatz' of a linear pressure dependence  $K = K_0 + K'_0 P$  as shown in the following,

$$\frac{1}{\rho} \frac{d\rho}{dP} = \frac{1}{K} \rightarrow \frac{1}{V} \frac{dV}{dP} = -\frac{1}{K} \rightarrow dP = -(K_0 + K'_0 P) \frac{1}{V} dV \quad (55)$$

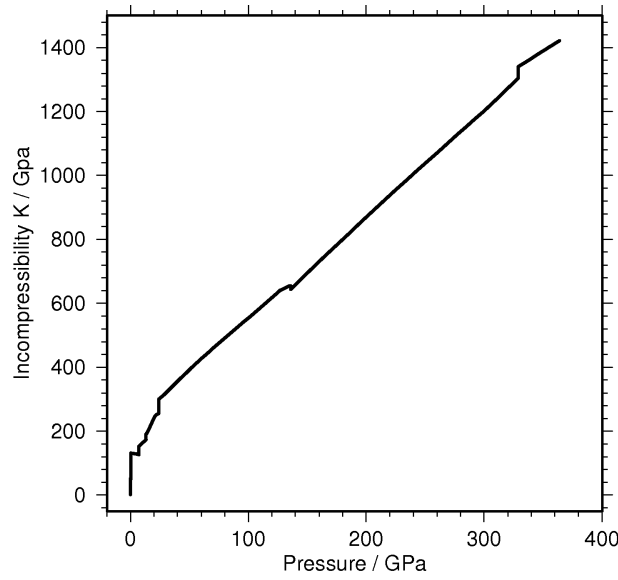


Figure 3: Incompressibility profile derived from the PREM model.

**problem: 21** Derive an explicit expression for the pressure dependent density from the Murnaghan equation of state (58).

Answer:

$$\rho(P) = \rho_0 \left( \frac{K'_0 P}{K_0} + 1 \right)^{1/K'_0} \quad (59)$$

**problem: 22** In problem 19 we have seen that a simple model with uniform incompressibility and gravity  $K = K_0$  and  $g = g_0$  leads to physically impossible solutions. In a refined version of this model, applied to the Earth's mantle,  $g = g_0$  is maintained (compare Fig.1), and  $K$  is parameterized using the powerlaw relation (54).

Derive the following density profile for the model corresponding to (54).

$$\rho(r) = \rho_0 \left( 1 + (n-1) \frac{\rho_0 g_0 z}{K_0} \right)^{\frac{1}{n-1}} \quad (60)$$

where  $z = R - r$  is the depth coordinate and the 0 subscript refers to zero pressure conditions. Note that the singularity for  $\rho_0 g_0 z / K_0 = 1$  in problem 19 is absent in this model.

$$\int_0^P \frac{dP'}{K_0 + K'_0 P'} = - \int_{V_0}^V \frac{1}{V'} dV' = \int_V^{V_0} \frac{1}{V'} dV' = \ln \left( \frac{V_0}{V} \right) \quad (56)$$

Substitution in the integral over pressure of  $K_0 + K'_0 P' = x$ ,  $dx = K'_0 dP'$  gives,

$$\int_{x_0=K_0}^{x_P=K_0+K'_0 P} \frac{1}{K'_0 x} dx = \frac{1}{K'_0} \ln \left( \frac{K_0 + K'_0 P}{K_0} \right) = \ln \left( \frac{V_0}{V} \right) \quad (57)$$

$$1 + \frac{K'_0 P}{K_0} = \left( \frac{V_0}{V} \right)^{K'_0} \rightarrow P = \frac{K_0}{K'_0} \left( \left( \frac{V_0}{V} \right)^{K'_0} - 1 \right) \quad (58)$$

This relation is known as the Murnaghan equation of state (EOS).

A more widely used and more accurate EOS for a higher pressure range is the equation derived by Birch (1952) from a consideration of elastic strain energy, known as the Birch-Murnaghan EOS (Poirier, 2000).

In other cases than the special simplified cases discussed above, in particular in problems 19 and 22, the gravity acceleration varies also with depth. Also more accurate equations of state may be necessary for very high pressure, encountered in the deep interior of large (exo)planets, that result in large compression. Such models can be formulated in a more general way by the following coupled set of equations for pressure, gravity and density.

$$\frac{dP}{dr} = -\rho g \quad (61)$$

$$g(r) = \frac{Gm(r)}{r^2} \quad (62)$$

$$F(\rho, P, T) = 0 \quad (63)$$

where the radial mass distribution  $m(r)$  is defined as in (31). A model based on (61), (62), and (63) can be constructed for the internal structure (density, gravity, pressure) of a planet of given mass  $M$  and composition, i.e. with given parameters of the EOS (63) such as  $\rho_0, K_0, K'_0$  in the Murnaghan EOS (58). Consider the application of such a model to a planet for which only the planet mass  $M$  is known.<sup>11</sup> Assume a homogeneous terrestrial (rocky) planet without a distinct metallic core. Assuming an earth-mantle like composition, representative values of the EOS parameters can be used, to solve the coupled model equations in the following iterative scheme.

1. Define a grid along the radial coordinate  $r_i, i = 1, \dots, N, r_1 = 0$ . This grid defines a subdivision of the interior in  $N - 1$  concentric layers and must be chosen large enough, i.e.  $r_N > R$ .
2. Choose an initial estimate of the central pressure  $P^{(1)}(0)$ .
3. In a loop over the internal layers, starting upward from the centre, first compute the pressure decrement over the layer from (61). This is then used to obtain the pressure at the next grid point and corresponding density from the EOS (63). From the computed density the corresponding mass distribution  $m(r_i)$  and gravity  $g(r_i)$  (62) follow.
4. The layer iteration in the previous item is stopped when a zero pressure value has been reached. The radial level reached this way now defines the next approximation of the planetary radius  $R^{(j)}$  and  $M^{(j)} = m(R^{(j)})$  is a new approximation of the planet mass  $M$ .
5. From the total mass defect  $\Delta M^{(j)} = M^{(j)} - M$  a correction to the central pressure is computed as  $\Delta P^{(j)}$ , (problem 23). In the next iteration the radial integration is repeated from item 3 with an updated central pressure  $P^{(j+1)}(0) = P^{(j)}(0) + \Delta P^{(j)}$  and this iterative procedure is repeated until convergence is reached, i.e. until  $|\Delta M^{(j)}|/M$  drops below a specified tolerance value.

---

<sup>11</sup>Such models can be applied to exoplanets that are recently being discovered [wikiMethods\\_of\\_detecting\\_extrasolar\\_planets](#). For some of these planets, detected from radial velocity variations of the star, only the planet mass  $M$  is known.

**problem: 23** A correction for the central pressure in item 4 can be estimated by distributing the mass defect  $\Delta M^{(j)}$  over a spherical shell of thickness  $\Delta R^{(j)}$ , positioned at the surface, and computing an approximate pressure  $\Delta P^{(j)}$  at the bottom of this shell.

Derive the following expression for the thickness of this spherical shell,

$$\frac{\Delta R^{(j)}}{R^{(j)}} = \left( \frac{\Delta M^{(j)}}{M^{*(j)}} + 1 \right)^{1/3} - 1 \quad (64)$$

Where  $M^{*(j)} = \frac{4\pi}{3}\rho(R^{(j)})R^{(j)3}$ .

The correction for the central pressure is then defined as,  $\Delta P^{(j)} = \rho(R^{(j)})g(R^{(j)})\Delta R^{(j)}$ .

### 2.6.3 Adiabatic density distribution

In the previous section density models were based on assumptions about the parameterization of the bulkmodulus  $K$ . The density model of Williamson and Adams (1923), (Hemley, 2006) does not depend on a parameterized  $K$ . Instead it is defined in terms of the seismic wave velocities  $v_p$  and  $v_s$  that can be determined from inversion of seismological traveltime data as  $K/\rho = v_p^2 - 4/3v_s^2$ .

The W-A model can be derived from thermodynamic principles for a homogeneous self-compressing layer which is in an adiabatic state. The bulkmodulus applied in this model is expressed in the seismic wave velocities which in turn depend on the elasticity parameters and the density. The elastic deformation proces in seismic wave propagation occurs on a relatively short time scale (seconds-minutes) compared to the characteristic time scale of conductive heat transport in solids (see 3.3). Therefore (diffusive) heat exchange can be neglected and adiabatic conditions apply in seismic wave propagation. This implies that the elasticity parameters determined from seismic data, including the bulkmodulus  $K$  pertain to adiabatic conditions (see also Appendix A.3).

Other processes such as convective mantle flow that occur on a much longer time scale may take place under more general (non-adiabatic) conditions.

In section 3 on the thermal state of the Earth it is shown that adiabatic conditions hold for the interior of a fluid layer when heat transport is dominated by advection and heat diffusion by conduction/radiation plays a minor role. Assuming the Earth's mantle to be in a state of vigorous thermal convection it also follows that the average temperature profile, the geotherm, corresponds to an adiabatic distribution.

In general the density differential can be written as,

$$d\rho = \left( \frac{\partial \rho}{\partial P} \right)_S dP + \left( \frac{\partial \rho}{\partial S} \right)_P dS \quad (65)$$

where the differential of the entropy  $S$  is dropped in case of adiabatic conditions and the pressure derivative is written in terms of the adiabatic bulkmodulus  $K_S$  defined in (45),  $1/K_S = (\partial \rho / \partial P)_S / \rho$ .

**problem: 24** Derive the Williamson-Adams equation for a homogeneous adiabatic layer from the density differential (65) and assumption of isentropic (adiabatic) conditions with  $dS \equiv 0$ ,

$$\frac{d\rho}{dr} = -\frac{\rho^2 g}{K_S} \quad (66)$$

The density solution of the W-A equation can be expressed in terms of the seismic parameter  $\Phi = K_S/\rho$  which in turn can be obtained from seismic velocity models:  $\Phi = v_p^2 - \frac{4}{3}v_s^2$  for  $P$  and  $S$  waves.  $\sqrt{\Phi} = \sqrt{K_S/\rho}$  is known as the bulkvelocity. For a given bulkvelocity profile, obtained from seismic observations, the W-A density profile is derived from (66) as,

$$\ln \left( \frac{\rho(r)}{\rho(R)} \right) = \int_r^R \Phi^{-1}(r')g(r')dr' \quad (67)$$

**problem: 25** Derive (67) by integration of the W-A equation (66).

In (67) the gravity acceleration  $g$  depends on the density distribution  $\rho(r)$  in the lefthand side. Therefore the density profile can not be simply obtained from a seismologically determined  $\Phi(r)$  profile and a single evaluation of the integral in (67). The expression represents an integral equation that can be solved iteratively as specified in problem 26.

**problem: 26** Assume that a seismic parameter profile for the mantle  $\Phi(r)$ , obtained from seismic travel times, is available. Investigate how (67) can be used to compute a sequence of mantle density profiles  $\rho^{(j)}(r), j = 1, 2, \dots$  in an iterative procedure, by successive substitution. How would you define a starting profile  $\rho^{(1)}(r)$  for this iterative procedure?

*Hint: Substitute the density profile for iteration number  $j$  in the gravity acceleration in the righthand side of (67) for the computation of an updated profile  $j + 1$ . This is an example of a general solution strategy for non-linear problems known as ‘successive substitution’ or Picard iteration.*

Williamson and Adams (1923) used the iterative scheme in problem 26 to test the hypothesis that the mass concentration towards the Earth’s centre is completely explained by compression of a homogeneous self-gravitating sphere. They showed that integrating (67) from a surface value of  $3.3 \cdot 10^3 \text{ kg/m}^3$  results in unrealistically high density values for depths greater than the core-mantle boundary. This way they concluded that an inhomogeneous earth with a dense, compositionally distinct core, probably iron-nickle, was required by the observations. The necessary multiple integrals in the evaluation of (67) had to be computed by means of graphical approximation methods in 1923, several decades before the advent of electronic computers.

In a later analysis Bullen (1936) showed that the assumption of a homogeneous selfcompressing mantle described by the W-A equation, and a chemically distinct dense core, leads to unrealistically high values of the moment of inertia for the core  $I_c = fM_cR_c^2$ , with a prefactor value  $f \sim 0.57$  greater than the value of a core with uniform density, 0.4. Since this would imply a density decrease towards the centre Bullen concluded that the applicability of the W-A model for the whole mantle can not be maintained and that instead a distinct mantle transition layer, labeled C-layer, must be included between the upper and lower mantle proper, related to transitions in mineral phase and/or composition (Bullen, 1975).

**problem: 27**

1. Derive the following equation for the temperature distribution of a W-A layer (see Appendix A.3),

$$\frac{dT}{dr} = -\frac{\alpha g}{c_P}T \quad (68)$$

where  $\alpha$  and  $c_P$  are the thermal expansion coefficient and the specific heat at constant pressure.  
Hint: Use the differential for the entropy,

$$dS = \left(\frac{\partial S}{\partial T}\right)_P dT + \left(\frac{\partial S}{\partial P}\right)_T dP \quad (69)$$

and the thermodynamic relations:  $(\partial S/\partial T)_P = c_P/T$  and  $(\partial S/\partial P)_T = -\alpha/\rho$ .

2. Derive the expression for the temperature profile for an adiabatic layer, sometimes referred to as the ‘adiabat’, by solving equation (68),

$$T(r) = T(R) \exp\left(\int_r^R \frac{\alpha g}{c_P} dr'\right) \quad (70)$$

The temperature extrapolated to the surface,  $T_P = T(R)$  is known as the potential temperature of the layer. The quantity  $H_T = (\alpha g/c_P)^{-1}$  is known as the thermal scale height of the layer.

3. Derive an expression from (70) for the special case with a constant value of the scale height parameter.

The W-A equation for the density of an adiabatic layer can be generalized introducing the Bullen parameter  $\eta$  which is used as a measure of the departure of the actual density/temperature profile from an adiabat. This is done by writing,

$$\eta(r) = -\frac{\Phi}{\rho g} \frac{d\rho}{dr} \quad (71)$$

where  $\eta(r)$  has been substituted for the constant value ( $\equiv 1$ ) in the W-A equation.

## 2.7 Current density models

The concept of an adiabatic layer was essential when no independent determinations for the density distribution were available and the W-A equation was used to compute  $\rho(r)$  for given values of the seismic parameter  $\Phi(r)$  determined from seismological observations (Bullen, 1975).

During the 1970s a radial density distribution has been obtained for the Earth from inversion of seismological observations, incorporating spectral analysis of the Earth’s eigenvibrations, under the constraints of the given values for  $M$  and  $I$ . This, together with seismic velocities determined from bodywave traveltimes and surfacewave dispersion, has resulted in the Preliminary Reference Earth Model (PREM), (Dziewonski and Anderson, 1981).

Since  $\rho(r)$  can be determined from analysis of the earth’s normal modes (radial eigenvibrations) the ‘adiabaticity’ of the mantle is no longer assumed.

The degree of ‘adiabaticity’ is used in numerical modelling experiments as a diagnostic for the dynamic state - where a high degree of adiabaticity indicates vigorous thermal convection and predominantly convective heat transport (van den Berg and Yuen, 1998, Matyska and Yuen, 2000, Bunge et al., 2001).

Usually the outcome of such experiments shows that the upper and lower mantle separately are approximately adiabatic - away from boundary layers where conductive transport dominates. In recent years models of the deep lower mantle have become popular where a compositionally distinct dense layer occupies the bottom 30% (roughly) of the lower mantle (Kellogg et al., 1999, Albaredo and van der Hilst, 2002).

## 2.8 Earth's chemical composition

For a complete description of the Earth's interior we need to know its chemical composition, temperature and pressure. In section 2.3 the pressure is expressed in the density distribution and the related internal gravity field. Once the internal pressure distribution is known, sharp transitions or discontinuities in the material properties, like the seismic velocities  $v_p$ ,  $v_s$  and the density in the PREM model, can be identified with mineral phase transitions and as such they can be related to the mineral ( $P, T$ ) phase diagram of candidate mantle silicate materials in order to estimate the temperature in the Earth's interior. Such phase diagrams are determined from experimental (HPT) and theoretical work in mineral physics.

What do we know about Earth's bulk chemical composition? Candidate mantle materials have been defined based on cosmochemical and petrological considerations. Models of the chemical composition of the Earth are commonly based on the hypothesis that the planet was formed in a multi-stage accretion process from material that condensed from the original solar nebula approximately 4.6 billion years ago at the time of formation of the solar system. The chemical composition of chondritic meteorites, in particular the carbonaceous chondrites (CI type) (McBride and Gilmour, 2003) show a strong correlation with the composition of the outer layer of the sun (photosphere), determined from spectral analysis of the solar light, as illustrated in Fig. 4 (Anders and Grevesse, 1989).

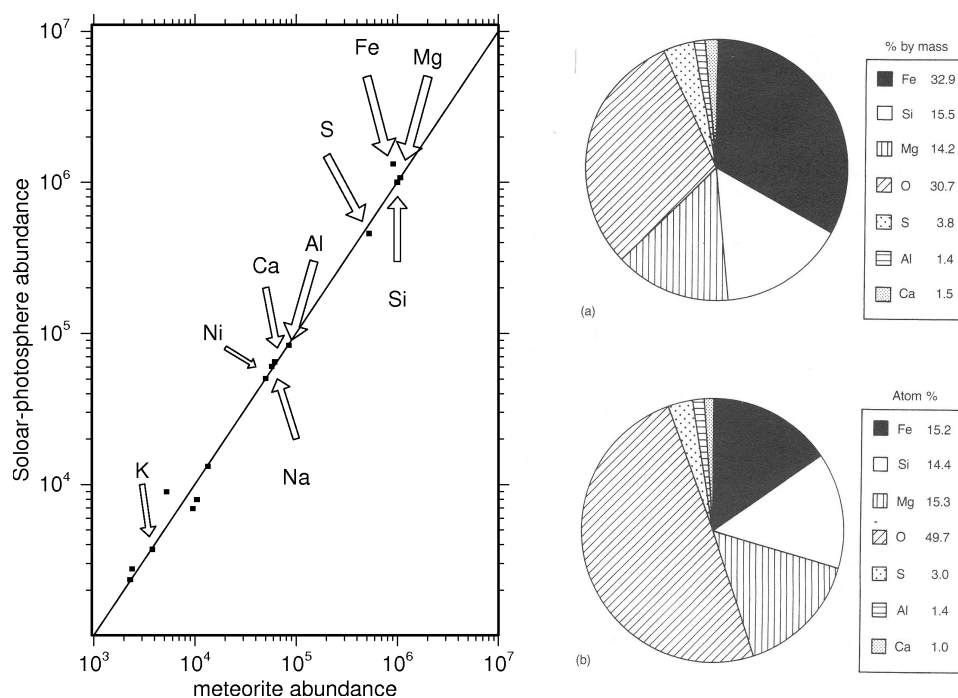


Figure 4: *Left: Element abundance (normalized with  $Si = 10^6$ ), of the solar shallow photosphere compared to chondritic meteorites (Anders and Grevesse, 1989). Right: amounts of Earth's major elements assuming a chondritic composition (Brown and Musset, 1993).*

The solar-chondritic data in the lefthand frame show that Mg, Fe and Si are by far the most abundant (non-volatile) elements. According to the chondritic Earth hypothesis a similar abundance

can be expected for the bulk-earth. This is illustrated in the righthand pie diagrams. Note the large proportion of oxygen, bound in oxides. In most crust-mantle rocks S is less abundant than Al or Ca. This is usually explained by assuming that S is relatively volatile and also ‘siderophile’, meaning that a significant fraction may have ended up in the iron-nickel core during an early core-mantle differentiation.

The chondritic meteorites are thought to be representative of the undifferentiated material condensed from the solar nebula.

Around 1960 a model chemical composition for the bulk of the Earth’s mantle, coined pyrolite, was introduced by Ringwood (see (Ringwood, 1975) and original references therein). This is still used as a reference model. The pyrolitic composition is associated with the main upper mantle rock type peridotite that is brought to the Earth’s surface in small fragments included in volcanic rocks (xenoliths) and also in larger, kilometer sized, fragments in so called peridotite bodies (Spengler et al., 2006). The pyrolitic composition of the upper mantle rocks is also strongly correlated with the composition of chondritic meteorites, in agreement with the hypothesis of a chondritic origin of the Earth.

Mantle peridotites are found with different degrees of depletion (mass fraction lost) by partial melting. More depleted material is denoted as harzburgite and the relatively undepleted peridotite is known as lherzolite. During progressive partial melting the mineral composition of the residual rock material, a mineral assemblage consisting of olivine, pyroxene and garnet, shifts towards the olivine composition. The olivine enriched harzburgitic residue appears to be the chemical complement of the basaltic melt product, with respect to the original lherzolitic mantle source rock. This depletion relation, between oceanic and continental crust on the one hand and peridotitic mantle rock on the other, is reflected in the element abundance of crust and mantle rocks, illustrated in Fig. 5.

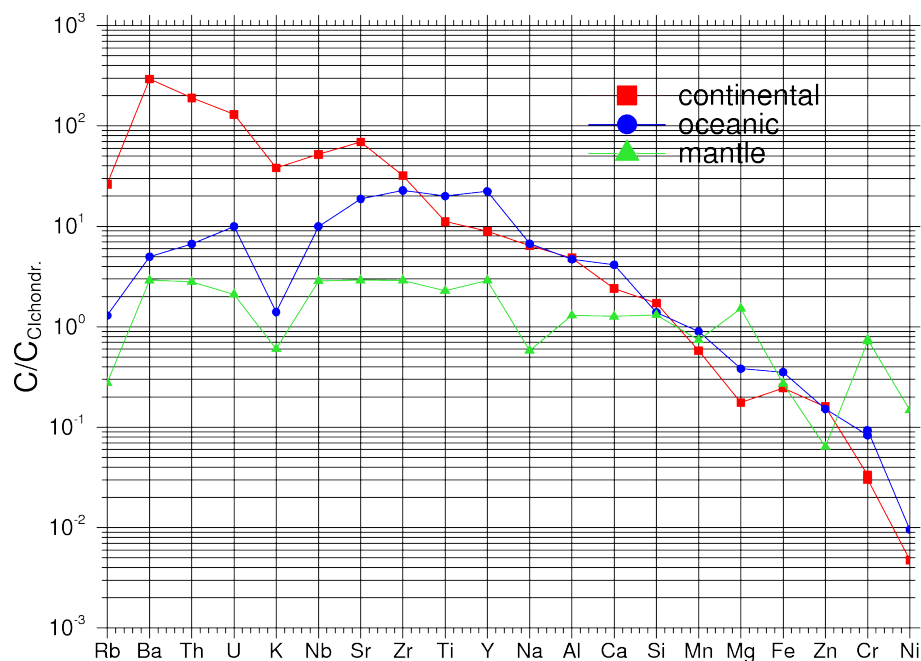


Figure 5: Chemical abundance of crustal and mantle rocks, normalized with respect to CI chondritic values. Data from (McBride and Gilmour, 2003).

This figure shows abundance ratio's relative to the CI-chondritic composition. The curve for mantle rock appears to be relatively close to the chondritic composition, whereas the crustal material is enriched with respect to the mantle in most elements shown.

A notable exception to this crustal enrichment is found for magnesium which appears to be enriched in average mantle peridotite. This is in agreement with the previous observation that the olivine/pyroxene content ratio of the residual increases with the degree of partial melting. Magnesium content increases with the olivine (forsterite  $\text{Mg}_2\text{SiO}_4$ )/pyroxene  $\text{MgSiO}_3$  ratio.

An other observation that can be made from Fig. 5 is the apparent depletion of the siderophile elements Fe and Ni, both in crust and mantle material, with respect to the chondritic composition. This is usually explained by the formation of a liquid Fe, Ni rich metal core of the Earth during the first few million years of the accretion proces, in the early solar system. During this event the molten liquid metal would have differentiated from the silicate mantle, leaving the mantle depleted in siderophile (iron loving) elements.

Core formation is also sometimes used as an explanation of the apparent K (potasium) depletion of both mantle and crust with respect to chondrites. In this explanation K is dissolved in liquid iron in significant quantity at high pressure and temperature (Rama Murthy et al., 2003). An alternative explanation for the Earth's K depletion is an escape of K due to significant volatilization during the planetary accretion proces.

**problem: 28** *From Figure 5 it can be concluded that the Earth's mantle and crust lost roughly 2/3 of its original iron content corresponding to a chondritic composition. Verify how this iron-depletion of crust and mantle could be explained by differentiation of the Earth's mostly-iron core. Use the following data in your argument: a) The mass fraction of the core  $X_c = M_c/M_\oplus = 0.315$ . b) The Fe mass fraction  $X_{mFe} \sim 10\%$  of the pyrolitic mantle, c) The mass fraction of lighter elements in the core - (S, Si, O) amounts to about 20%. d) The Fe mass fraction of the bulk Earth  $X_{\oplus Fe} \sim 33\%$  (Fig. 4)*

## 2.9 Phase transitions as anchor points of the geotherm

Major phase boundaries in the Earth’s mantle and core have been identified with sharp transitions in the seismic wave velocities and the density distribution of the PREM model shown in Fig. 1.

The depth distribution of the mineral composition for a pyrolitic mantle model is shown in Fig. 6. This figure clearly illustrates the different mineral composition of the upper and lower mantle regions separated by the major phase boundary near 660 km depth ( $\sim 24$  GPa), where the ringwoodite polymorph of olivine,  $(\text{Mg, Fe})_2\text{SiO}_4$ , transforms (dissociates) into a mineral assemblage of perovskite,  $(\text{Mg, Fe})\text{SiO}_3$  and magnesiowüstite,  $(\text{Mg, Fe})\text{O}$ .

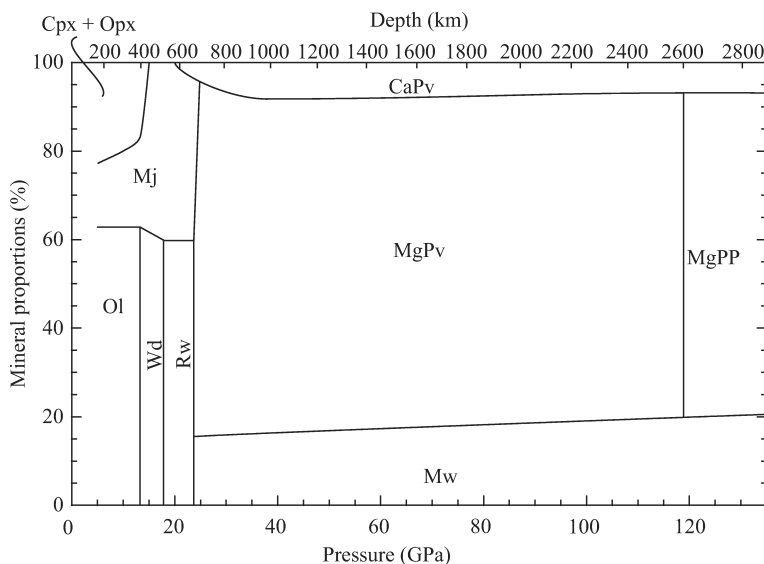


Figure 6: *Pressure/depth distribution of mineral assemblage for a pyrolitic mantle model. Cpx: clinopyroxene, Opx: orthopyroxene, Mj: majorite garnet, Ol: olivine, Wd: wadsleyite, Rw: ringwoodite, CaPv:  $\text{CaSiO}_3$  perovskite, MgPv:  $\text{MgSiO}_3$ -rich perovskite, MgPP:  $\text{MgSiO}_3$ -rich post-perovskite, Mw: magnesiowüstite. (From: (Hirose, 2007))*

For a given mantle composition, for instance for a pyrolitic mantle, the pressure-temperature mineral phase diagram can be determined for the relevant  $P, T$  range of the Earth’s mantle by HPT experiments and mineral physics theory. A sharp transition at a pressure  $P_t$  in the PREM model can then be located at the corresponding pressure in the phase diagram by the intersection of the  $P_t$  isobar with the diagram phase boundaries. The (possibly multiple) intersection points define the corresponding transition temperature  $T_t$ . The pressure-temperature point located in the phase diagram defines an ‘anchor point’ that constrains the geotherm. In this procedure the phase transition is used as a mantle/core thermometer.

This way several  $(P, T)$  ‘anchor points’ of the geotherm have been determined, related to the solid state phase transition near 660 km depth and the solid/liquid inner/outer core boundary at 1220 km from the Earth’s centre.

Fig. 7 from (Boehler, 1996) illustrates the determination of anchor points of the geotherm at the phase boundary near 660 km depth ( $P_{660} = 24\text{GPa}$ ,  $T_{660} = 1900 \pm 100$  K) and at the boundary between the outer and inner core at 5150 km depth, ( $P_{ICB} = 330\text{GPa}$ ,  $T_{ICB} = 4850 \pm 200$  K).

Starting from these anchor points the temperature is then extrapolated from both sides to the core mantle boundary at 2900 km depth. For this temperature extrapolation assumptions have to be made about the dominant heat transport mechanism and in this case it is assumed that heat transport operates mainly through thermal convection. This will be further investigated in later sections dealing with heat transport in the Earth's mantle.

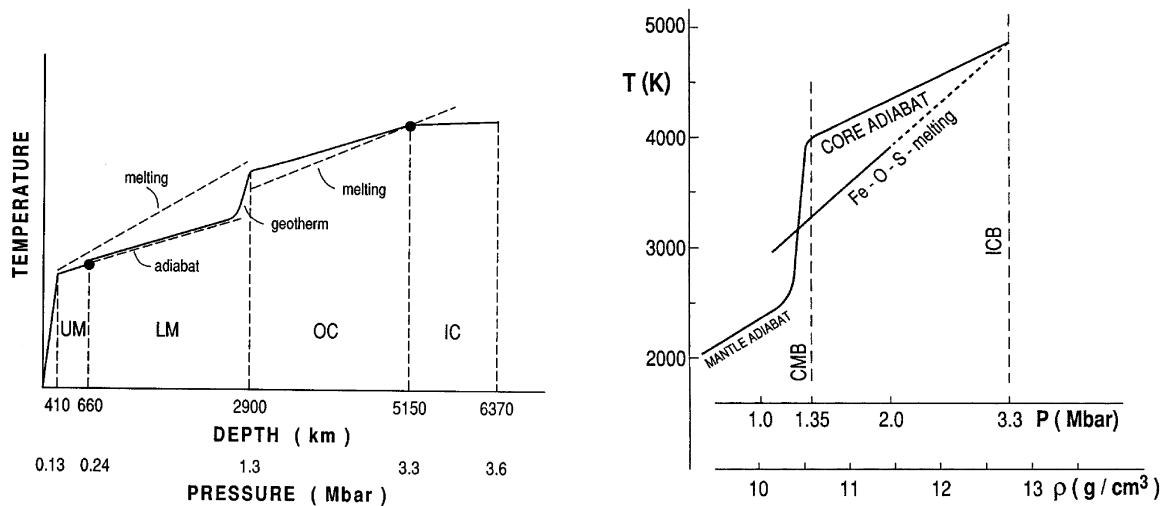


Figure 7: Schematic radial temperature distribution in the mantle and core, constrained by major phase transitions (Boehler, 1996), (UM-upper mantle, LM lower mantle, OC outer core, IC inner core). The temperature of the upper/lower mantle boundary is constrained by the  $\gamma$ -spinel to postspinel phase transition at 660 km depth. The temperature at the inner/outer core boundary at 5150 km depth (radius 1220 km) is constrained by the melting temperature of the hypothetical core 'Fe-O-S' alloy. The right hand frame shows a schematic core temperature distribution (geotherm) labeled 'CORE ADIABAT' in the liquid outer core versus pressure and the melting curve (liquidus) of the core 'Fe-O-S' alloy. (CMB core-mantle boundary, ICB inner core boundary). The ICB is determined by the intersection of the liquidus and the geotherm. During core cooling the ICB moves outward as the inner core grows by crystallisation.

**problem: 29** Estimate the temperature near the bottom of the mantle by adiabatic extrapolation of the temperature  $T_{660} \sim 1900\text{K}$  of the phase transition near 660 km depth, to the depth of the core mantle boundary, using the general expression for the adiabat in a homogeneous layer.

Hints: apply the result of problem 27 and assume uniform values of the 'scale height parameter'  $H_T = (\alpha g/c_P)^{-1}$ , with  $\alpha = 2 \cdot 10^{-5}\text{K}^{-1}$ ,  $g = 10\text{ms}^{-2}$ ,  $c_P = 1250\text{Jkg}^{-1}\text{K}^{-1}$ . Further: approximate the adiabat by a linear depth function, in agreement with the schematic diagram of Fig. 7, to obtain a uniform adiabatic temperature gradient.

The 'head' of the extrapolated outer core adiabat is at a temperature of approximately 4000 K and the 'foot' of the lower mantle adiabat at approximately 2700 K. This result indicates a large temperature contrast of about 1300 K across the CMB.

How can such a large contrast be explained physically? As we will see later, this can be explained by interpreting the CMB as a boundary between two separately convecting fluid layers, each with

a thermal boundary layer where the main heat transport mechanism shifts from convection in the interior of the fluid layers, to conduction near the boundary interface, where vertical convective transport vanishes with the flow velocity component normal to the boundary. Separately convecting layers are in agreement with the large density contrast across the CMB where the density almost doubles, as illustrated in Fig. 1. The resulting strong temperature contrast across the CMB is consistent with a lower mantle in a state of vigorous thermal convection.

**problem: 30** *Explain why we can not turn this argument around and conclude from these indications for a strong temperature contrast at CMB that the mantle convects vigorously.*

*Hint: Check Appendix A.3 for the assumptions made for an adiabatic geotherm in the lower mantle.*

More recent developments, providing independent information, shed new light on the temperature distribution in the bottom layer of the lower mantle. A previously unknown mantle phase transition has been identified, in the main constituent magnesium-perovskite, to a ( $\sim 1.5\%$ ) denser phase (post-perovskite) both in experimental HPT and theoretical (mineral physics) work at temperatures and pressure conditions corresponding to a region in the lowermost mantle close to the core-mantle boundary. This is illustrated in Fig. 8, showing experimental data points delineating the phase boundary.

This phase transition has a high valued positive slope of the phase boundary (Clapeyron parameter)  $dP_t/dT \sim 10 \text{ MPaK}^{-1}$ . The intercept of the phase boundary with the core mantle boundary at  $\sim 136 \text{ GPa}$  appears to be at a temperature several hundred Kelvin below the temperature of the liquid metal outer core as illustrated in Fig. 8. As a consequence the geotherm may intersect the phase boundary at multiple depth's, depending on the local mantle temperature, a phenomenon known as 'double crossing' (Hernlund et al., 2005). When a double crossing of the geotherm occurs, a thin layer exists directly bordering the core, where perovskite is the stable phase while on top of this bottom PV layer, a postperovskite layer exists with a variable thickness of up to several hundred kilometers.

A further implication of the phase diagram illustrated in Fig. 8 is that the PPV layer will be absent in hot regions where the geotherm is completely above the PV-PPV phase boundary. This post-perovskite phase boundary has also been associated with the top of the D'' layer at variable height  $\sim 100 - 300 \text{ km}$  above the CMB (Lay et al., 2005).

These seismological interpretations of the postperovskite phase boundary have been based on limited resolution methods applying 1-D radial velocity models. In a more recent development, techniques related to seismic wave migration methods, used in the oil and gas exploration industry, are applied to delineate reflecting interfaces in 2-D and 3-D models in seismic stratigraphy of the CMB region (van der Hilst et al., 2007). This way the spatial resolution has been brought down to about 20 km, allowing mapping of detailed structures in the lowermost mantle. An important target of these high resolution seismic methods is the bottom interface of a postperovskite layer, associated with the 'double crossing', where mantle material transforms back from postperovskite into perovskite due to the steep increase in temperature in the bottom thermal boundary layer, illustrated in Fig 8, related to the temperature contrast across the CMB.

In a similar way as for the spinel-postspinel phase transition the temperature at the seismic interfaces can then be estimated from the given depth(pressure) and the experimentally determined parameters of the postperovskite phase transition. This way a mantle adiabatic geotherm and boundary layer structure (error function) have been estimated with a CMB temperature  $T_{cmb} \sim 4000 \text{ K}$  (van der Hilst et al., 2007). The 'foot' of the adiabatic mantle geotherm derived from this lies at a temperature of approximately 2500 K. Both the estimated CMB temperature and the foot of the

adiabat seem to confirm independent earlier findings based on adiabatic temperature extrapolation over large depth ranges (Boehler, 1996).

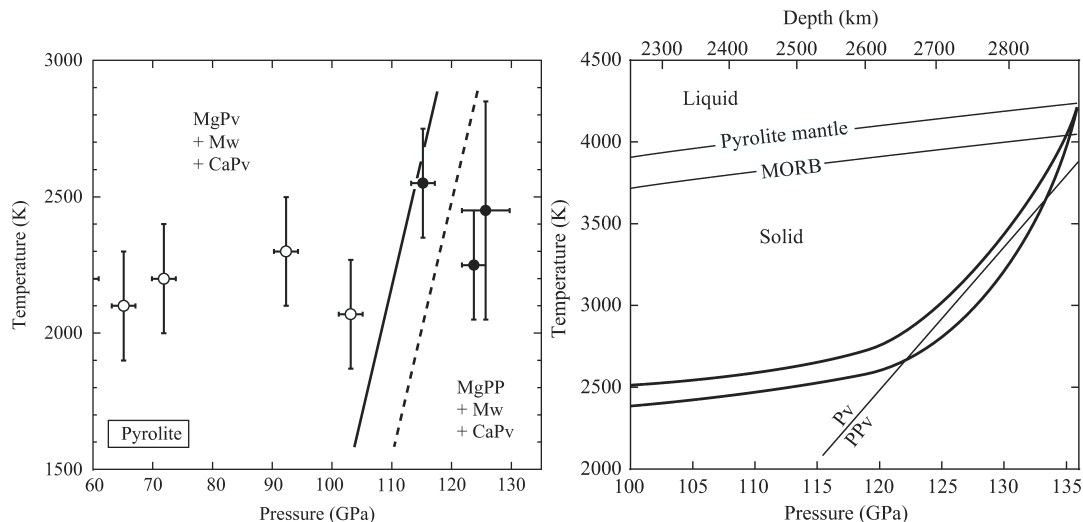


Figure 8: *Left: phase relations near the bottom of the mantle for pyrolitic material (Hirose, 2007). The solid- and dashed line correspond to different pressure calibration of the HPT experiments. The Clapeyron slope of the phase boundary is assumed 11.5 MPa/K. CaPv:  $\text{CaSiO}_3$  perovskite MgPv:  $\text{MgSiO}_3$ -rich perovskite, MgPP:  $\text{MgSiO}_3$ -rich post-perovskite, Mw: magnesiowüstite. Right: schematic temperature profiles in the lower mantle in relation to the perovskite (Pv) to postperovskite (PPV) phase transition and the melting curve for pyrolitic mantle material and subducted basaltic crust (MORB) (Hirose, 2007).*

The temperature contrast of about 1500 K across the core-mantle boundary resulting from these interpretations identify the bottom of the mantle as a thermal boundary layer, characteristic of a vigorously convecting layer where the boundary interface has a fixed or slowly varying temperature, as we will see in the section on heat transport in the mantle. As such these results from mineral physics and seismology have produced new evidence for strong mantle convective flow near the core-mantle boundary.

### 3 Thermal state of the Earth

#### 3.1 Introduction

Earth can be considered as a heat engine, where the flow of energy out of the system into the environment, space, controls the internal dynamics of the system, this is manifested in the long term existence of a magnetic field and in surface processes which are directly or indirectly observable in the geological record. From the eighteenth century on, the thermal state of the Earth's interior has been the subject of investigation. In the nineteenth century, the discrepancy between the age of the Earth estimated from simple physical, conductive cooling models and the time scales apparently involved in geological processes was a source of great controversy that lasted until the discovery of natural radioactive decay and the realisation that this process could be a significant source for internal heating of the Earth.<sup>12</sup>

In the twentieth century the role of solid-state (sub-solidus) thermal convection in the Earth's mantle became an issue, directly related to the concepts of continental drift described by Wegener. This issue was settled in the 1960s when plate-tectonics became established, based on marine-geophysical paleomagnetic observations. Thermal convection is much more effective in removing heat from the interior of a hot planet than thermal conduction in representative mantle silicate material. In current geophysical models for the thermal state of the Earth the global heat-output, estimated at  $44 \cdot 10^{12}$  W or 44 TW, consists for the larger part of the heat involved in cooling the oceanic plates, continuously formed at ocean ridges.

The potential temperature<sup>13</sup> of the Earth's upper mantle is an important parameter which controls the process of pressure release partial melting in hot upwelling mantle flows. This process is essential in the creation of basaltic crust at oceanic spreading ridges, as part of the present day plate tectonics. During Earth's thermal evolution the uppermantle temperature has decreased and the melting conditions in the hotter 'young' Earth may have been such that a much thicker lithospheric layer of basaltic crust and underlying depleted (buoyant) peridotite was formed than today. As a result the conditions for gravitational instability of the cooling oceanic crust/lithosphere would have been quite different from today's, resulting in a geodynamic regime different from today's large scale plate tectonics and characterized by a smaller scale more chaotic type of circulation (Vlaar and van den Berg, 1991, Vlaar et al., 1994, van Thienen et al., 2004, van Hunen and van den Berg, 2008).

As shown in section 2.9 the present day temperature distribution in the Earth's interior is constrained by a number of phase transitions, illustrated schematically in Fig. 7. The solid-state phase transition from the  $\gamma$  spinel (ringwoodite) polymorph of olivine  $(\text{Mg, Fe})_2\text{SiO}_4$  to the 'post-spinel' assemblage of  $(\text{Mg, Fe})\text{SiO}_3$  (perovskite) and  $(\text{Mg, Fe})\text{O}$  (magnesiowüstite) has been observed experimentally at 23.9 GPa and  $1900 \pm 100$  K (Boehler, 1996)

Similarly the melting point of iron at conditions for the inner/outer core boundary at 330 GPa has been determined by Boehler at  $4850 \pm 200$  K for pure iron. The actual temperature may be slightly lower due to the eutectic effect of lighter elements sulfur and oxygen in the liquid. Extrapolation of the temperature from the inner core boundary along an outer core adiabat gives an estimate of the temperature at the core-mantle boundary, slightly higher than 4000 K.

The thermal evolution and present state of the core is of direct importance for the geodynamo process which generates the Earth's magnetic field through thermo-chemically driven convection in

<sup>12</sup>ref. section 1.3 *History of ideas about the Earth* in: (Brown and Musset, 1993) and (Holmes, 1915).

<sup>13</sup>See problem 27.

the liquid outer core. Gravitational energy is released through chemical differentiation during inner core crystallization. The residual liquid layer around the inner core is enriched in the lighter elements, most likely sulfur, oxygen, silicon. The resulting gravitational instability drives the chemical convection. This is estimated to be a greater power source for the dynamo than the latent heat release associated with the inner core crystallization, (Loper, 1978).

The history of the magnetic field is preserved in rock samples dating back to the archaean era (4-2.5 Gyr b.p.). These data suggest that the magnetic field existed at 3.5 Gyr b.p. On the other hand, theoretical work and modelling studies suggest that the inner core started crystallizing at a later time than 3.5 Gyr b.p. (Buffet, 2003). This implies that in the early Earth power sources must have been available, other than the formation energy of the inner core, to drive the dynamo by purely thermal convection only. Possibly radiogenic potassium  $^{40}\text{K}$ , with its relatively short half life time could have played this role in the early Earth. Hypothetical  $^{40}\text{K}$  segregation into the core during core mantle differentiation, which occurred in the first few million years in the early Earth, would also provide a partial explanation, for the depletion from the mantle and crust with respect to a chondritic (reference) composition by a factor of seven. This  $^{40}\text{K}$  enrichment of the core could have happened in combination with loss of K due to volatilization, during the early accretion stages of planet formation, (Rama Murthy et al., 2005).

In the following, contributions in the Earth's heat budget are considered in more detail and put in perspective with the Earth's thermal evolution.

### 3.2 Earth's heat output

An inventory of the Earth's global heatflux is given in Table 2. The regional/local situation may deviate from the global averages in the table in particular depending on the local tectonical regime involving for instance age-dependence in oceanic plates or areas with regional volcanism.

Continent	$Q_{cont}$	$2 \cdot 10^8 \text{km}^2 \times 65 \text{mW/m}^2 = 13 \cdot 10^{12} \text{W}$
Ocean	$Q_{oc}$	$3.2 \cdot 10^8 \text{km}^2 \times 101 \text{mW/m}^2 = 31.3 \cdot 10^{12} \text{W}$
Global heatflow	$Q$	$44.2 \cdot 10^{12} \text{W}$
Global heatflowdensity	$q$	$87 \text{mW/m}^2$

Table 2: *Inventory of global heatflow after Pollack et al., 1993.*

The distribution of the surface heatflow density with major contribution from young oceanic regions is illustrated in Fig. 9.

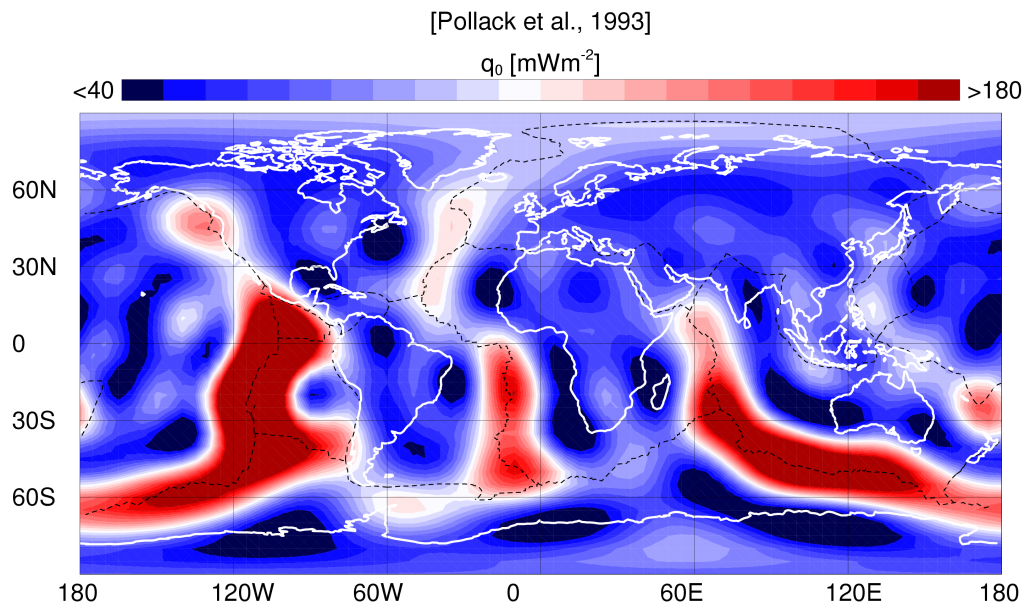


Figure 9: *Global distribution of surface heatflow density after (Pollack et al., 1993).*

### 3.3 The Earth's energy budget and energy transport mechanisms

Several important factors which determine the Earth's present thermal state and thermal evolution are summarized in the following:

1. *The initial temperature of the Earth's thermal evolution*

This was established during the accretionary phase of the Earth's formation at the time of formation of the solar system about 4.6 Gyr before present. Dissipation of kinetic energy from impacts during the early bombardment period probably resulted in high internal temperatures, leading to substantial melting and initiation of core/mantle differentiation.

Compaction due to increasing self-gravitation and resulting pressure build-up during accretion results in dissipation of gravitational potential energy and a rise of internal temperature.<sup>14</sup>

The differentiation of an iron/nickel core from an earlier homogeneous configuration probably took place within the first several tens of million years. As a result the gravitational potential energy released during core segregation in such a relatively short period would have melted most of the silicate mantle, creating a global magma ocean.

The formation of the moon by a giant collision of a 'mars-sized' body with the proto Earth, in the same time window of the first few tens of million years of the Earth's evolution, has further increased the internal temperature, evaporating part of the mantle.

A direct record of these events is lacking because the oldest observed rocks are about 4 billion years old. Mainly indirect evidence, for instance from geochemical trace element analysis, is used to constrain the dating of these early events like core formation.

Because of the remaining uncertainties about the earliest 'Hadean' period of Earth's history (4.6-4 Gyr b.p.) the initial temperature is sometimes taken as an adjustable parameter in models of thermal evolution of the Earth, starting from the early Archean period about 4 billion years b.p. This parameter is then adjusted such that the present day global heatflux corresponds to the estimate of  $\sim 87\text{mW/m}^2$  based on available heatflow measurements (Pollack et al., 1993).

2. *Internal heat sources*

The most important sources for internal heating are radiogenic heat production, discussed in section 3.4.1, and release of gravitational energy, at present the main driving mechanism of thermo-chemical convection in the outer core. To a lesser extent, latent heat from phase transitions (mainly crystallization of the inner core), contributes to the heat source budget.

3. *Effective heat transport processes*

The thermal state depends strongly on the effective heat transport mechanisms. Thermal conductivity of mantle silicates is quite low,  $k \sim 4\text{Wm}^{-1}\text{K}^{-1}$ .<sup>15</sup> This corresponds to a thermal diffusivity  $\kappa \sim 10^{-6}\text{m}^2\text{s}^{-1}$  which means that the (diffusional) thermal relaxation time,  $\tau = h^2/\kappa$ , of a silicate layer with the thickness of the Earth's mantle ( $h$ ) is several orders of magnitude greater than the age of the Earth.

---

<sup>14</sup>In an ideal elastic medium the gravitational energy would be stored as mechanical (potential) energy that could be recovered during (elastic) expansion. In practice there will be dissipation resulting from anelastic effects that leads to internal heating.

<sup>15</sup>([wiki/List\\_of\\_thermal\\_conductivities](#)) Thermal conductivity in  $\text{Wm}^{-1}\text{K}^{-1}$ : air  $\sim 0.025$ , diamond 2000  $\sim$  2500, granite 1.7 - 4.0, copper 353 - 386.

Sub-solidus thermal convection by means of solid state creep flow is the main transport mechanism to remove the Earth's internal heat on a geological time scale. In section 3.5 a number of thermal evolution models are introduced where both transport processes have been included and the relative efficiency of convective and conductive heat transport is investigated.

### 3.4 Internal heating by natural radioactive decay

#### 3.4.1 Radiogenic heating in a chondritic earth

The ratio of the instantaneous global internal heat production rate and the global heatflux through the Earth's surface is known as the Urey ratio ( $Ur$ ). Assuming a chondritic composition for the Earth (Ringwood, 1975, Brown and Musset, 1993), in the 1950s it seemed that the estimated surface heatflux could be completely accounted for by chondritic internal heating, (see section 3.4.2) corresponding to a unit Urey ratio, (MacDonald, 1959). Since that time the total observed heatflux through the Earth's surface has been updated several times based on an increased number of heatflow measurements and is nowadays estimated to be significantly greater than the chondritic internal heating value.

In the following a rough estimate of the global heatbudget is given involving  $Ur < 1$ . To this end we first consider a reference configuration with  $Ur = 1$  where the global heatflux and chondritic internal heating are exactly balanced. From the numbers in Table 2 we can then calculate the corresponding heatproduction rate per unit mass as,

$$A_a = \frac{Q}{M_{\oplus}} = \frac{44.2 \cdot 10^{12} \text{W}}{6 \cdot 10^{24} \text{kg}} = 7.37 \cdot 10^{-12} \text{W/kg} \quad (72)$$

This value of  $A_a$  is close to the characteristic value of  $(3 - 5) \times 10^{-12} \text{W/kg}$ , reported for chondritic meteorites. However this similarity is coincidental as we will see.

Since we wish to relate the surface heatflux  $Q$  to an average heatproductivity for the mantle  $A_M$ , we have to correct the above calculation of the contributions for the crust and the core. As a first approximation we assume the radiogenic heatproduction in the core to be negligible. In that case we only need to correct for the mass of the core in the above estimate. Since  $M_{core}/M_{mantle} \approx 1/2$  we obtain,

$$A_m^{(1)} = \frac{3}{2} \times 7.37 \cdot 10^{-12} \text{W/kg} \quad (73)$$

In a further refinement we correct this number for the heat productivity of the crust only, the mass of the crust can be neglected here. The heat produced in the oceanic crust can be neglected in comparison with the heat produced in the continental crust. A common assumption is that about half of the continental heatflow is generated in the crust. Since the Earth's crust is about 2/5 continental it follows that 1/5 of the global heatflow originates from the continental crust. This results in a heatproduction rate per unit mass, corrected for the core and crust,

$$A_m^{(2)} = \frac{4}{5} \times \frac{3}{2} \times 7.37 \cdot 10^{-12} \text{W/kg} = 8.8 \cdot 10^{-12} \text{W/kg} \quad (74)$$

This value is higher than the chondritic value. By assuming that the difference (about 40%) is provided by secular cooling of the earth, ( $Ur = 0.6$ ), the global heat flux can be rationalized with the chondritic earth model.

### 3.4.2 Heat production rates in representative rocks

The assumption of a core without radiogenic heat sources in the previous section is uncertain. There is not much evidence of uranium U or thorium Th in the core but the possibility of significant potassium K has been suggested as a possible explanation of the K depletion of both crust and mantle rocks with respect to chondritic meteorites. This is expressed in the K/U ratio which is around  $7 \times 10^4$  for the chondrites and  $10^4$  for crust/mantle rock.

Alternative explanations for the crust/mantle depletion of K are 1) the volatile character of K which may have resulted in the escape of vaporized material in degassing events during Earth's hot early stages and 2) significant solubility of K in liquid iron which could have resulted in K partly washing out of the mantle during segregation of the core. Recently it has been shown, using improved experimental techniques (Rama Murthy et al., 2003), that contrary to earlier experimental results, K can be put in solution in liquid iron in significant quantities at high temperature and pressure. Therefore radiogenic K in the earth's core could provide part of the power required by the geodynamo, especially in the early stages of evolution before the solidification of the inner core had started and the heat productivity of K, with its relatively short half-lifetime of 1.25 Gyr was much more dominant in Earth's radiogenic fuel-mix (compare Fig. 10).

An impression of the distribution of radiogenic heatproduction is obtained from xenolites.<sup>16</sup> Xenolites sample the mantle to depths of several hundred kilometer. Data for representative rock types are given in Table 3. An average chondritic composition is included to put the data in perspective with the *chondritic earth model*.

Rocktype	U (ppm)	Th (ppm)	K (%)	K/U
Chondritic meteorites	0.008	0.029	0.056	$7 \cdot 10^4$
Peridotite - lherzolite (undepleted reference mantle)	0.031	0.124	0.031	$10^4$
Peridotite - harzburgite (depleted mantle)	0.001	0.004	0.003	$3 \cdot 10^3$
Average continental crust	1.42	5.6	1.43	$10^4$
Shale	3.7	12	2.7	
Granite	4.7	20	4.2	
Tholeiitic basalt (mid-ocean ridge basalt MORB)	0.07	0.19	0.088	

Table 3: *Isotope concentrations for several important rocktypes, after Turcotte and Schubert (2001).*

To bring the data in Table 3 in line with the chondritic earth model one can assume that the uppermantle (sampled by the xenolites) is enriched in U, Th and K with respect to the average mantle and furthermore that the mantle is depleted in K with respect to the chondritic composition.

It is clear from these data that granite provides the highest heat productivity and that the oceanic crust (tholeiitic basalt) produces little radiogenic heat (3%, versus 97% from cooling). The oceanic crust is enriched with respect to its source rock lherzolite, while the melt residu harzburgite is depleted with respect to the source rock in agreement with the complementary character of both rock types. These trends are in agreement with Fig. 5, illustrating the complementary nature of crust and upper mantle with respect to chondritic meteorites.

<sup>16</sup>Solid rock fragments, typically centimeter sized, contained in magma flows from the mantle.

Due to natural radioactive decay the concentration of the different radioactive isotopes in the Earth's interior is time dependent. Assuming the concentration at the present time  $C_0$ , the concentration at  $t$  time units back in the past is,

$$C(t) = C_0 \exp(\lambda t) \quad (75)$$

where the decay constant  $\lambda$  is related to the half-life  $\tau_{1/2}$  as  $\lambda = \ln(2)/\tau_{1/2} = 0.69/\tau_{1/2}$ .

In natural rocks a 'fuel-mix' of, say  $N$ , different radiogenic isotopes is present, each with its characteristic half-life time. The heat production rate per unit mass in this case is represented as the cumulative effect of the individual  $N$  isotopes,

$$H(t) = \sum_{j=1}^N H_j(t) = \sum_{j=1}^N A_j C_j(t) = \sum_{j=1}^N A_j C_{0j} \exp(\lambda_j t) \quad (76)$$

where the  $A_j$  are the heat production rates per unit mass of the (pure) individual isotopes. A time-varying 'effective half-life time' and corresponding decay constant  $\lambda$  can be derived for a given fuel-mix from the above defined by,

$$\frac{dH}{dt} = \lambda H(t) \quad (77)$$

The effective decay constant  $\lambda(t)$  is,

$$\lambda(t) = \frac{\sum_{j=1}^N \lambda_j A_j C_{0j} \exp(\lambda_j t)}{\sum_{j=1}^N A_j C_{0j} \exp(\lambda_j t)} = \sum_{j=1}^N \lambda_j \left( \frac{H_j(t)}{H(t)} \right) \quad (78)$$

The effective  $\lambda$  increases (the corresponding  $\tau_{1/2}$  decreases) with  $t$  (going back in time) in agreement with the early predominance of short lived isotopes in the decaying fuel-mix.

The half-life times of the relevant isotopes are very different. For  $^{238}\text{U}$  and  $^{232}\text{Th}$  they are much longer than for  $^{235}\text{U}$  and  $^{40}\text{K}$  as shown in Table 4.

Isotope $j$	$A_j$ (pure isotope) W/kg	$\tau_{1/2j}$ yr	$C_j$ kg/kg	$H_j = C_j A_j$ $10^{-12}\text{W/kg}$
$^{238}\text{U}$	$9.46 \cdot 10^{-5}$	$4.47 \cdot 10^9$	$30.8 \cdot 10^{-9}$	2.91
$^{235}\text{U}$	$5.69 \cdot 10^{-4}$	$7.04 \cdot 10^8$	$0.22 \cdot 10^{-9}$	0.125
U	$9.81 \cdot 10^{-5}$		$31.0 \cdot 10^{-9}$	3.04
$^{232}\text{Th}$	$2.64 \cdot 10^{-5}$	$1.40 \cdot 10^{10}$	$124 \cdot 10^{-9}$	3.27
$^{40}\text{K}$	$2.92 \cdot 10^{-5}$	$1.25 \cdot 10^9$	$36.9 \cdot 10^{-9}$	1.07
K	$3.48 \cdot 10^{-9}$		$31.0 \cdot 10^{-5}$	1.07

Table 4: *Isotope parameters after Turcotte and Schubert (2001). The present day composition of free uranium is 99.27 %  $^{238}\text{U}$  and 0.72 %  $^{235}\text{U}$ .  $C_j$  are estimated present day average mantle values, corresponding to Table 3.*

The heating rates per unit mass for the average mantle composition, ( $H_j$ ), can be extrapolated backwards in time from the present, using the isotope data in Table 4. The result of such an extrapolation is shown in Fig. 10.

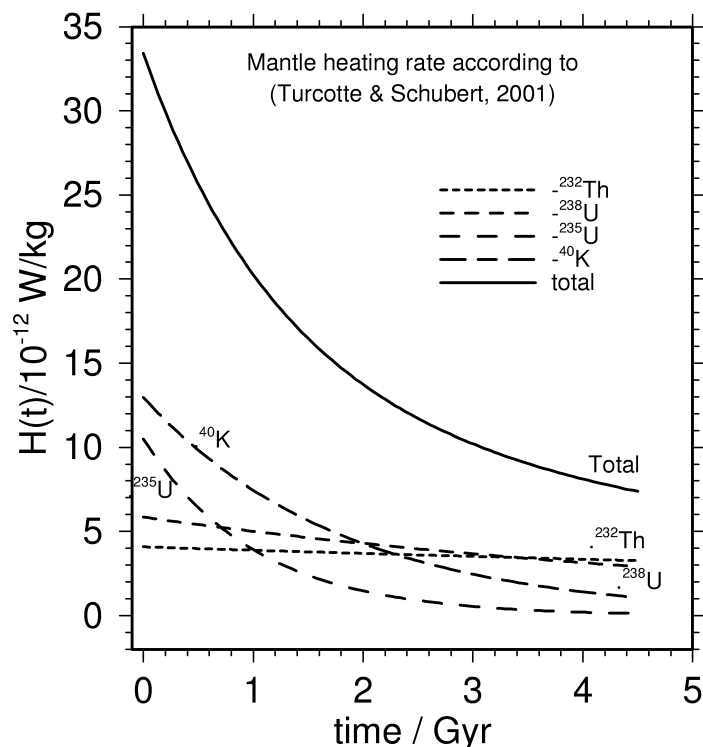


Figure 10: *History of internal heating rate per unit mass for an average mantle composition according to Turcotte and Schubert (2001) (solid curve), decomposed in the individual isotope contributions, (dashed curves).*

Figure 10 shows that the internal heating rate from radioactive isotopes was substantially higher, two to three times, during early periods of the Earth's history like the Archean (4-2.5 Gyr b.p.) and almost a factor of five if we extrapolate the data back to the earliest part of the Hadean period (4.5-4Gyr b.p) the time of planetary formation. During the early history the 'short lived' isotopes  $^{40}\text{K}$  and  $^{235}\text{U}$  were the main heatproducing elements and also  $^{26}\text{Al}$  may have been important. This in contrast to the present day situation where  $^{232}\text{Th}$  and  $^{238}\text{U}$  produce most of the radiogenic heat.

Combining Table 3 and 4 we get a table of present day heating rate numbers for the important rock types listed in Table 5.

Table 5 illustrates the fact that the heat producing elements are 'incompatible', meaning that these elements are preferentially concentrated in the melt during partial melting of mantle rock. This way the radiogenic elements concentrate in a liquid (melt) film in the interstitial pore space of the (low porosity < 1 %) porous mantle rock, from where they are transported to the surface in a melt segregation process. As a result mantle rock, continuously recycled in the mantle geodynamical recycling process, will get more depleted in radiogenic elements over time. The incompatible elements accumulate in the continental crust which has a high concentration of radiogenic heat sources.

Table 5 shows that the continental crustal rocks have by far the highest internal heating rate. Granitic rocks are representative for the upper continental crust.

**problem: 31** Determine the thickness of an equivalent granitic layer that could produce all of the continental heatflow. Assume  $\rho = 2.7 \cdot 10^3 \text{ kg/m}^3$  for the rock density.

**Answer:** 23 km.

Apparently the average thickness of the ‘granitic’ layer is thinner than the quoted 23 km and a commonly used estimate for the continental lithospheric heatflow is that about 50% consists of heat generated in the (upper) crust where the rest mainly consist of mantle heat entering the lithosphere from the deeper mantle.

For oceanic lithosphere the situation is different. Although internal heating of the basaltic crust is much lower than for the continental crust, the available heat from the cooling spreading lithosphere results in a higher average surface heatflow density compared to the continental crust as shown in Table 2 and illustrated in Fig. 9. Apart from the higher average value, the observed oceanic heatflow density varies with the (thermal) lithospheric age, in agreement with conductive cooling models for a column of lithosphere moving horizontally away from the spreading oceanic ridge.

Rocktype	Heat production rate $10^{-12} \text{Wkg}^{-1}$
Chondrites	3.5
Granites	1135
Tholeitic basalt (MORB)	15
Peridotite - harzburgite (depleted)	0.3
Peridotite - lherzolite (undepleted)	7.4

Table 5: Heat production rates for several rocktypes.

### 3.5 Thermal evolution models

From geological evidence it has been concluded that the Earth has cooled since the early archaean, 4 Gyr b.p., by an uncertain amount, possibly upto several hundred centigrade. The occurrence of komatiites (magnesium rich meltproduct of peridotite), almost exclusively formed during the archaean period, provides indications about the temperature of the upper mantle in the early Earth. Extrusion temperatures of upto 1650 centigrade have been derived, slightly higher than the zero pressure melting temperature. The temperature in the source region of these melts at depths of at least 200 km is estimated at 1750 centigrade.

#### 3.5.1 Parameterized evolution models

In the following a simple model is introduced for the volume average temperature of a cooling planet in order to put the available thermal energy and present day global heat transport in perspective.

We assume a specific heat value for the Earth as a whole  $c_P = 800$  J/kg/K and average temperature values and mass values for the mantle and core,

$$\langle T \rangle_m = 2273 \text{ K}, \quad \langle T \rangle_c = 4273 \text{ K}, \quad (79)$$

$$M_m = 4 \cdot 10^{24} \text{ kg}, \quad M_c = 2 \cdot 10^{24} \text{ kg} \quad (80)$$

This amounts to a bulk thermal energy  $E \sim Mc_P T$  of  $1.4 \cdot 10^{31}$  J. The present day global surface heatflow, listed in Table 2, is  $Q = 44.2 \cdot 10^{12}$  W. The ratio of these numbers is known as the Kelvin time of the system  $\tau_K = E/Q = 1.4 \cdot 10^{31}/44.2 \cdot 10^{12} = 3.16 \cdot 10^{17}$  sec = 10 Gyr. This represents a first, rough estimate of the thermal relaxation time of the Earth, illustrating that the Earth is a very slowly evolving thermal system.

The rough estimate in the above can be improved by applying a conservation law for thermal energy to derive an evolution equation for the average temperature  $\langle T \rangle$ . By volume integration of the energy equation, see Appendix A.2, the following equation for the average temperature is obtained,<sup>17</sup>

$$C \frac{d}{dt} \langle T(t) \rangle = -Q(t) + H(t) \quad (81)$$

In (81) the total heat capacity of the system is defined as,

$$C = \int_V \rho c_P dV \quad (82)$$

and the averaged temperature, weighted by the local heat capacity, as

$$\langle T(t) \rangle = \frac{1}{C} \int_V \rho c_P T dV \quad (83)$$

The total internal heat production rate of the system is defined as,

$$H = \int_V H_v dV \quad (84)$$

where  $H_v$  is the local volumetric internal heating rate, defined as the product of the heating rate per unit mass and the density  $\rho H_m$ .

---

<sup>17</sup>In contrast to the convention in the previous section, the time variable  $t$  increases with the model evolution in (81).

**problem: 32** *The simple model calculation leading to the estimated Kelvin time  $\tau_K \sim 10$  Gyr can be extended by taking the delaying effect of internal heating into account in a similar (simplified) way. To this end apply (81) and substitute constant values for a) the Earth's heatflux  $44 \cdot 10^{12}$  W and b) chondritic internal heating rate  $5 \cdot 10^{-12} \text{Wkg}^{-1}$ . Derive the value of the constant cooling rate  $d\langle T \rangle / dt$ , in, Kelvin per  $10^9$  years, predicted by this model and compare the outcome with the original model without internal heating. Answer: 284 K/Gyr and 90 K/Gyr.*

The heatflux through the boundary surfaces - the earth's surface and the core-mantle boundary (in case of a model for the mantle only) is expressed as,

$$Q(t) = \int_{\partial V} \mathbf{q} \cdot \mathbf{n} dV \quad (85)$$

where the heatflow density vector is expressed by Fouriers law for heat conduction  $\mathbf{q} = -k\nabla T$ .

By assuming a parameterized relation between the surface heatflux and the volume average temperature,

$$Q(t) = f(\langle T \rangle) \quad (86)$$

(81) becomes an ordinary differential equation (ODE) that can be solved for a given internal heating model  $H(t)$  and initial condition  $\langle T(0) \rangle$ .

In the above definition of the Kelvin time the surface heatflux is taken to be a constant (present day) value, and the heating rate is assumed zero. This can be considered as a special (trivial) case of (85) and (86) where  $f$  is a constant parameter and the thermal history follows as a linear function of time.

An improved approximation is to assume the surface heatflux to be proportional to the contrast between the internal temperature and surface temperature  $T_s$ ,

$$Q(t) = \alpha (\langle T(t) \rangle - T_s) \quad (87)$$

with a constant coefficient  $\alpha$ . This approximates the behavior of a simple physical model of a hot fluid with approximately uniform temperature separated from the cooling outer surface by a conductive boundary layer. Assuming a linear temperature profile in the boundary layer of thickness  $l$ , the surface heatflow can be approximated as  $Q = Ak(\langle T \rangle - T_s)/l$ . Where  $A$  is the surface area,  $k$  is thermal conductivity.

Substitution of the parameterization (87) in (81) and assuming an initial temperature contrast  $\langle T(0) \rangle - T_s = T_0$  the following solution can be derived for the thermal evolution, expressed in the average temperature, <sup>18</sup>

$$\langle T(t) \rangle - T_s = T_0 \exp(-t/\tau) + \frac{1}{C} \int_0^t \exp((t' - t)/\tau) H(t') dt' \quad (88)$$

where the *exponential* thermal relaxation time in (88) is defined by the constant,

$$\tau = \frac{C}{\alpha} \equiv C \frac{\langle T(t) \rangle}{Q(t)} = \frac{E(t)}{Q(t)} \quad (89)$$

---

<sup>18</sup>The first term in the right hand side of (88) is a solution  $T_h$  of the homogeneous differential equation that satisfies the initial condition. The second term is a particular solution  $T_p(t)$ , with  $T_p(0) = 0$ . Such particular solutions can be found with the method of *variation of parameters*. To this end substitute  $T_p(t) = a(t)T_h(t)$  in the ODE (81) to derive a homogeneous ODE that can be solved for  $a(t)$ .

This definition of a relaxation time has a different interpretation than the one corresponding to the Kelvin time defined for the model based on the constant surface heat flux assumption, although the numerical values are the same,  $E/Q = 10\text{Gyr}$ . The first term in (88) represents the transient effect of the initial temperature, the second term gives the contribution from decaying radiogenic heat sources, integrated over the thermal history.

### 3.5.2 Convection models

Heat transport from the Earth's interior to the surface appears to operate mainly through thermal convection. For the Earth's mantle, conduction contributes significantly only in the thermal boundary layers near the core-mantle boundary and the Earth's surface (lithosphere).

The relative inefficiency of thermal conduction in mantle rock material can be illustrated clearly by the following thought experiment. Consider a purely conductive steady state model, i.e.  $\partial \cdot / \partial t = 0$ , of a spherically symmetric Earth of radius  $R$  and uniform thermal conductivity  $k$  and with constant and uniform internal heating with a chondritic value  $H = 5 \cdot 10^{-12} \text{Wkg}^{-1}$ .

**problem: 33** Apply the steady state assumption to (103) and derive the heat equation for an internally heated sphere in spherical coordinates,

$$\frac{k}{r^2} \frac{d}{dr} r^2 \frac{dT}{dr} + \rho H = 0 \quad (90)$$

Solve this equation and express the radial temperature profile in terms of the surface temperature  $T(R) = T_R$  and the internal heating rate  $H$  as,

$$T(r) = T_R + \frac{\rho H}{6k} (R^2 - r^2) \quad (91)$$

Draw a schematic graph of the temperature distribution. Assuming earthlike values for the parameters, taking  $k \sim 5 \text{WK}^{-1}\text{m}^{-1}$ , compute the temperature value in the centre and halfway between the centre and the surface as an approximation of the core mantle boundary. What do you conclude from the outcome in view of the estimations of the internal temperature of the Earth based on experimentally determined phase transitions presented in section 2.9. What is the corresponding value of the surface heatflux and how does this compare to the estimated present day heatflux of the Earth?

**problem: 34** The internal temperature in the model described in problem 33 will be lower if the available (chondritic) internal heating is not distributed uniformly but concentrated towards the outer surface. In a more detailed steady state conductive model we assume that internal heating is confined to an outer shell, in line with concentration of radiogenic isotopes in the outer regions of the Earth resulting from early differentiation processes. Define  $R_1$  as the radius of the inner spherical volume without internal heating and  $H_1$  the internal heating value of the outer region. Derive the following expression for the radial temperature distribution,

$$T(r) = T_R \left[ 1 + \frac{\rho H_1 R^2}{6k T_R} \left\{ 1 - \left(\frac{r}{R}\right)^2 + 2 \left(\frac{R_1}{R}\right)^3 \left(1 - \frac{R}{r}\right) \right\} \right], \quad r \geq R_1 \quad (92)$$

In this model the maximum temperature  $T_1$  is reached for radius  $r = R_1$  and the inner region,  $r \leq R_1$  is isothermal with  $T = T_1$ . Assuming the total amount of radiogenic isotopes corresponds to the chondritic value of problem 33, show that  $H_1 = H / \left[ 1 - (R_1/R)^3 \right]$  and derive for the maximum temperature contrast with the surface,

$$T_1 - T_R = \frac{\rho H R^2}{6k} \left\{ \frac{1 - \left(\frac{R_1}{R}\right)^2 + 2 \left(\frac{R_1}{R}\right)^3 \left(1 - \frac{R}{R_1}\right)}{1 - \left(\frac{R_1}{R}\right)^3} \right\} \quad (93)$$

Compare this result with the outcome of problem 33 and compute the maximum temperature for a ‘core/mantle’ case with  $R_1 = R_c$ . Verify that  $T_1 \leftarrow 0$  for  $R_1 \rightarrow R$ .

More complete models also include heat transport by means of material transport, as in convective flow processes, besides thermal conduction. In the following Rayleigh-Benard thermal convection models are considered that can explain the Earth’s thermal state, including the observed surface heatflux and an internal mantle temperature that is below the melting temperature of mantle peridotite.

The Earth’s mantle can be described in a simple convective model set up as a highly viscous layer cooled from above and heated both internally and from below. In such a model the earth’s surface and the core-mantle boundary can be represented by impermeable boundaries. From the theory of thermal convection in viscous fluids it is known that under certain conditions heat transport in such model systems takes place predominantly by thermal convection in the interior of the fluid layer. The convective heat transport increases when the viscosity of the fluid is decreased and also when the temperature contrast between the cooler top surface and the hotter bottom surface is increased.

In this model heat is transported conductively through the thermal boundary layers that develop at the top and bottom boundary. This process, known as Rayleigh-Benard convection was investigated theoretically by Rayleigh (1916), who showed in a linear stability analysis that two regimes can exist depending on the value of the non-dimensional Rayleigh number,

$$Ra = \frac{\rho g \alpha \Delta T h^3}{\kappa \eta} \quad (94)$$

where  $\rho$  is the fluid density,  $\alpha$  the thermal expansivity,  $g$  the gravity acceleration,  $\Delta T$  the temperature contrast across the layer,  $h$  the layer depth,  $\kappa = k/\rho c_P$  the thermal diffusivity, expressed in the thermal conductivity  $k$  and  $\eta$  is the viscosity of the fluid.

Rayleigh’s linear stability analysis (Turcotte and Schubert, 2001) shows that the fluid is at rest for *subcritical* values of the Rayleigh number,  $Ra < Ra_c$ , and thermal convection sets in for *supercritical* Rayleigh number values,  $Ra > Ra_c$ . The critical value  $Ra_c$  is a so called bifurcation point of the heat transport model. For many configurations, layers, boxes, spherical shells,  $Ra_c$  is of the order 1000 as illustrated in Fig. 11 for a 2D rectangular domain.

The efficiency of convective heat transport is expressed in the non-dimensional Nusselt number defined as the ratio of the effective surface heatflux  $Q$  over the conductive heatflux of a corresponding purely conductive layer,

$$Nu = \frac{Q}{Q_{cond}}, \quad Q_{cond} = k\Delta T/h \quad (95)$$

**problem: 35** Derive the above conductive heatflux, for a plane layer of depth  $h$  with a temperature contrast  $\Delta T$  between the top and bottom, without internal heating, from the one-dimensional steady state heat diffusion equation.

*Hint: consider the steady state case of the heat diffusion equation (103) for the special case of a homogeneous layer with uniform top and bottom temperature  $T_0$  and  $T_0 + \Delta T$  respectively.*

The critical phenomenon of the onset of thermal convection is illustrated in Fig. 11. Nusselt number values of steady state Rayleigh-Benard convection, derived from numerical modelling calculations, are plotted against the Rayleigh number. The Nusselt number is close to the unit value

for Rayleigh numbers below the critical value,  $Ra_c \in [500, 800]$ , indicating purely conductive heat transport. For high Rayleigh numbers  $Ra \sim 10^6$  this figure suggests that convective heat transport is more than an order of magnitude more effective than purely conductive heat transport.

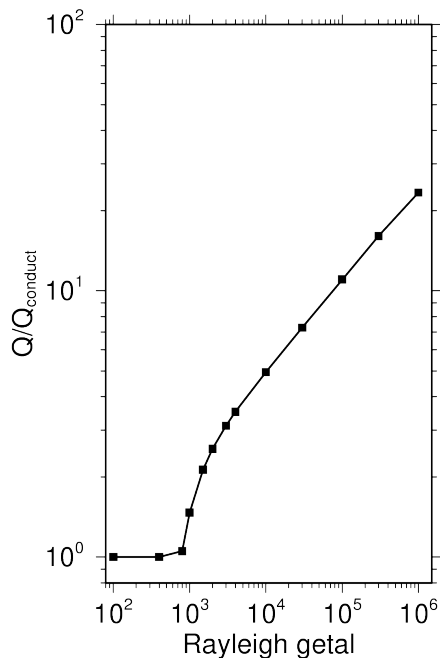


Figure 11: *Efficiency of convective heat transport measured by the Nusselt number as a function of the Rayleigh number, for an isoviscous fluid and a 2-D square domain, with freeslip impermeable boundaries. A powerlaw fit in the asymptotic regime for high Rayleigh number results in a powerlaw exponent of  $\beta = 0.35$ .*

Internal temperature distributions of several steady state convection models, compiled in Fig. 11, with contrasting Rayleigh numbers from  $10^4$  to  $10^6$  are illustrated in Fig. 12, showing the spatial distribution of the temperature  $T$  in the two-dimensional square domain and depth distribution of the horizontally averaged temperature - corresponding to a geotherm.

The different plot frames illustrate a ‘single cell’ convection pattern. The 2-D temperature distribution in Fig. 12 shows a hot plume rising from the isothermal bottom boundary and a cold downwelling limb of the convection cell sinking from the isothermal cold top boundary. Heat transport through the horizontal boundaries is controlled by thermal conduction, where the heatflow density vector is defined by Fourier’s law as  $\mathbf{J} = -k\nabla T$  (see Appendix A.1). It follows that the conductive heat flow increases with the increasing temperature gradient, corresponding to a decreasing thickness of the thermal boundary layers. This is also illustrated in the vertical profiles of the horizontally averaged temperature and is in agreement with the increase (factor  $\sim 5$  of the heat output between the cases with  $Ra$  is  $10^4$  and  $10^6$  respectively, indicated by Fig. 11.

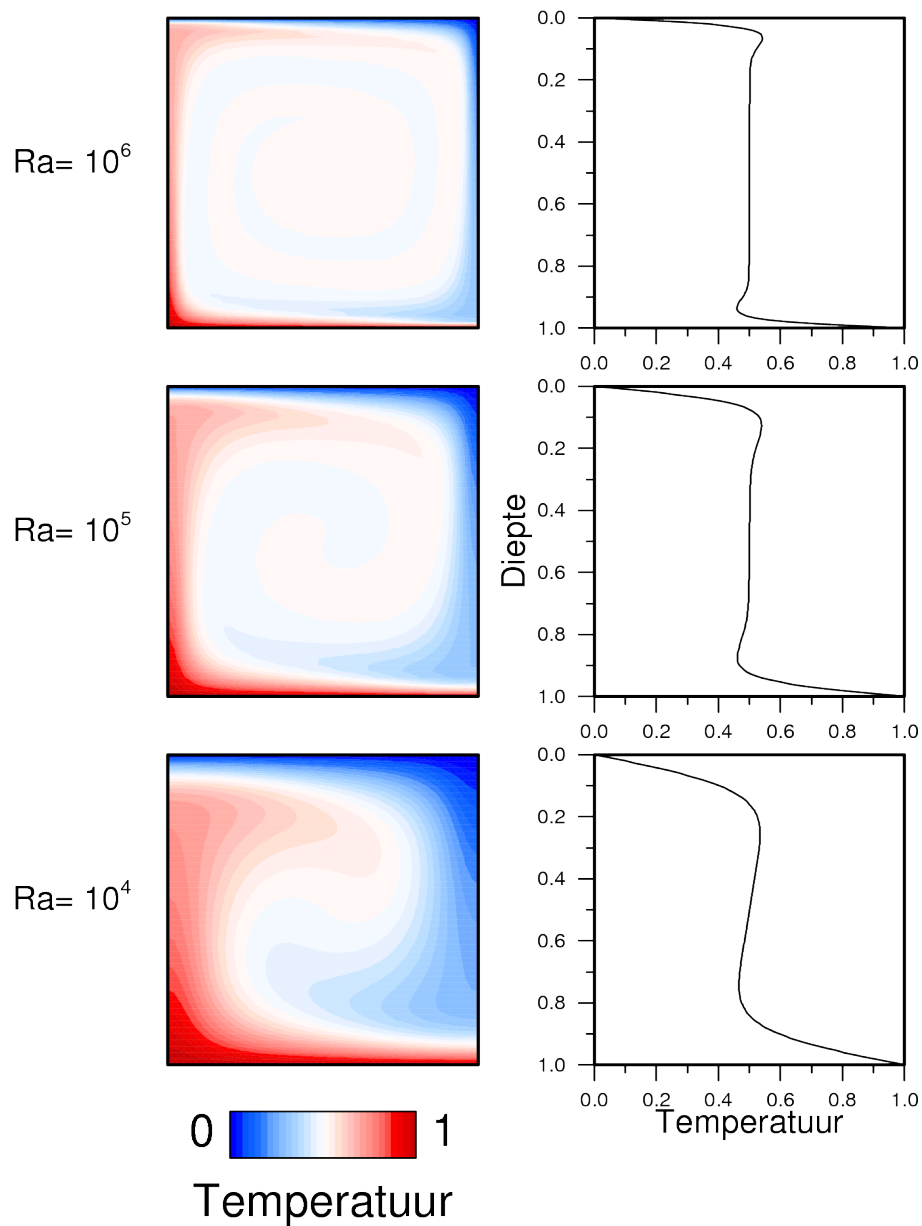


Figure 12: Numerical modelling results for 2-D steady state Rayleigh-Benard convection for different Rayleigh numbers  $10^4$  (bottom) to  $10^6$  (top). The left hand column shows the temperature distribution. The right hand column gives the vertical distribution of the horizontally averaged temperature. The temperature plots show an approximately isothermal core region of the convecting cell and thermal boundary layers at the top and bottom that become thinner for increasing Rayleigh number, explaining the trend in the Nusselt-Rayleigh number relation illustrated in Fig. 11.

**problem: 36** Use the approximate uniform parameters below, to compute estimated values of Rayleigh numbers of the following mantle configurations: (a) a whole mantle convection, (b) layered mantle convection with separate convecting layers in the upper- and lower mantle.

$\rho = 4.5 \cdot 10^3 \text{ kg/m}^3$ ,  $\alpha = 2 \cdot 10^{-5} \text{ K}^{-1}$ ,  $k = 4 \text{ Wm}^{-1}\text{K}^{-1}$ ,  $c_P = 1250 \text{ JK}^{-1}\text{kg}^{-1}$ ,  $\eta = 10^{22} \text{ Pa s}$ ,  $\Delta T_{\text{whole}} = 2000\text{K}$ ,  $\Delta T_{\text{upper}} = 1000\text{K}$ .

**Answer:**  $Ra_{\text{whole}} = 6 \cdot 10^6$ ,  $Ra_{\text{upper}} = 4 \cdot 10^4$ .

The values estimated above for the Rayleigh numbers of representative mantle layers suggest that the mantle is supercritical with respect to the onset of thermal convection. Combined with the Nusselt number data shown in Fig. 11 this implies that convective heat transport should be taken into account in thermal evolution considerations for planetary mantles.

Numerical experiments with thermal convection require the numerical solution of the time dependent (coupled) heat transport equations introduced in the Appendix. Global three dimensional cases of these so called full convection models on the scale of the mantle still represent a ‘computational challenge’. The reason for this is that for the high Rayleigh number values involved ( $Ra > 10^6$ ) the resulting time-dependent temperature field is characterized by small scale variations which require a high numerical resolution resulting in many degrees of freedom and long computation times.

For this reason thermal evolution models, taking into account convective heat transport have traditionally been so called parameterized convection models. These models have in common that the surface heat flux  $Q$  of the cooling body in (81) is parameterized. This is done by a parameterization of the heat transport characteristics of a convecting layer in terms of an asymptotic Nusselt-Rayleigh number relation, appropriate for high values of the Rayleigh number illustrated in Fig. 11 that can be derived from boundary layer theory (Turcotte and Schubert, 2001),

$$Nu = \left( \frac{Ra}{Ra_c} \right)^\beta \quad (96)$$

From the definition of the Nusselt number (95) it follows that the surface heatflow density  $q$  can be written as,

$$q = Nu \times q_{\text{cond}} = k \frac{\Delta T}{h} \left( \frac{Ra}{Ra_c} \right)^\beta \quad (97)$$

The surface heatflux  $Q$  follows by multiplication with the surface area,  $Q = q \times \int_{\partial V} dA$ . The power law exponent  $\beta$  can be determined from boundary layer analysis. For simple isoviscous layer cases this results in a value of  $\beta \sim 0.33$ . In these cases you also have  $\langle T \rangle = \Delta T/2$ , such that the surface heat flow density (97) can be written as,

$$q = \frac{k}{h} (2 \langle T \rangle)^{\beta+1} \left( \frac{\rho \alpha g h^3}{\eta \kappa Ra_c} \right)^\beta \quad (98)$$

Substitution of this expression for the surface heatflow density in (81) results in a differential equation for the time dependent volume averaged temperature of the cooling mantle.<sup>19</sup> Since the temperature of the early Earth is not well constrained, an often applied procedure is to integrate the equation backward in time from an estimate of the present day mantle temperature, for which values greater than 2000 K are used.

<sup>19</sup>This equation is non-linear and it is generally solved using a numerical integration method, for a given initial temperature in the early history of the Earth.

The formulation of parameterized convection models becomes more difficult for non-uniform physical parameters. The boundary layer analysis has been extended to media with temperature dependent viscosity where similar power law exponents of Nusselt-Rayleigh number relations are found. Substitution of a parameterization of the viscosity as a function of temperature  $\eta(T)$  can then be applied to implement the feedback effect of increasing viscosity during cooling which has a significant delaying effect on secular cooling of planetary mantles (Tozer, 1972).

Parameterizations of the temperature dependent viscosity based on the volume average temperature are typically of the form (Schubert et al., 1980, Jackson and Polack, 1984),

$$\langle \eta(T) \rangle = \eta_0 \exp\left(\frac{A}{\langle T \rangle}\right) \quad (99)$$

with parameter values, for the *limiting* ( $\langle T \rangle \rightarrow \infty$ ) kinematic viscosity  $\nu_0 = \eta_0/\rho = 2.2 \cdot 10^7 \text{ m}^2/\text{s}$  and the activation temperature  $A = 5.6 \cdot 10^4 \text{ K}$ .

For more general rheologies including also pressure and stress ( $\tau$ ) dependence,  $\eta(P, T, \tau)$  there are no such parameterizations available. In some of these cases parameterizations can be used based on an empirically determined power law Nusselt-Rayleigh number relation. This can be done by numerical experiments, solving the steady state heat transport equations numerically for a series of Rayleigh numbers in the range of interest, as in the numerical experiments resulting in Fig. 11 and determining the power law exponent  $\beta$  from the results by a regression (curve fitting) operation (van den Berg and Yuen, 1998).

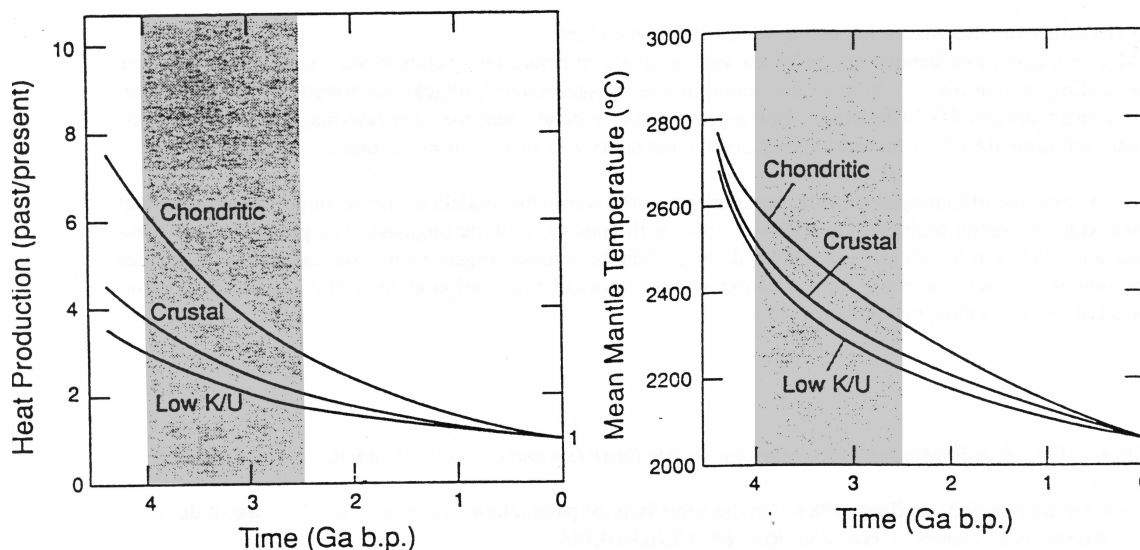


Figure 13: *Parameterized convection results (Pollack, 1997) for the thermal evolution of the mantle. Left: evolution of the normalized internal heating rate for different choices of the  $Th, U, K$  fuel mix. Right: average mantle temperatures corresponding to the different heating scenario's.*

A further limitation is related to the uniform thermal conductivity which underlies the parameterized models. In recent years it has been suggested that the mantle conductivity profile exhibits a conductivity minimum at shallow depth in a low conductivity zone (LCZ) (Hofmeister, 1999, van

den Berg et al., 2005). This is comparable to the low-viscosity zone of the mantle asthenosphere. This LCZ results from the fact that the major contribution of crystal lattice vibrations to the thermal conductivity decreases with increasing temperature and increases with increasing pressure, a similar situation as with the effective viscosity of the mantle rock. The net effect of the LCZ is an increase of the thermal resistance of the thermal boundary layer which results in a significant delay in secular cooling of one to two billion years, compared to corresponding models with uniform conductivity.

Fig. 13 illustrates the results of a typical example of a thermal evolution modelling experiment, investigating the impact of different internal heating scenarios on the average mantle temperature during the archean period (Pollack, 1997).

### 3.5.3 The role of solid state phase transitions in convective heat transport

The heat transport of a single Rayleigh-Benard convection cell can be described with a simple power law relation between the Nusselt and Rayleigh numbers. This is used in section 3.5.2 to parameterize the surface heatflux in terms of the internal temperature in calculations of thermal evolution. In the Earth's mantle the simple Rayleigh-Benard convection cell is only a first approximation. One of the complicating factors is the occurrence of several solid state phase transitions in the mantle transition zone between approximately 400 and 700 km depth. In particular the endothermic phase transition near 24 GPa, 1900 K of the  $\gamma$ -spinel (ringwoodite) polymorph of the main mantle constituent olivine  $(\text{Mg, Fe})_2\text{SiO}_4$  to the post-spinel assemblage perovskite  $(\text{Mg, Fe})\text{SiO}_3$  and magnesiowuestite  $(\text{Mg, Fe})\text{O}$  is thought to have an influence on large scale mantle convective flow, which promotes some form of layering in the circulation around a depth of 660 km (24 GPa pressure).

In contrast to this the other main phase boundary from  $\alpha$  olivine to the  $\beta$ -spinel (wadsleyite) polymorph of olivine at approximately 410 km depth is exothermic and has a de-stabilizing effect on mantle circulation.

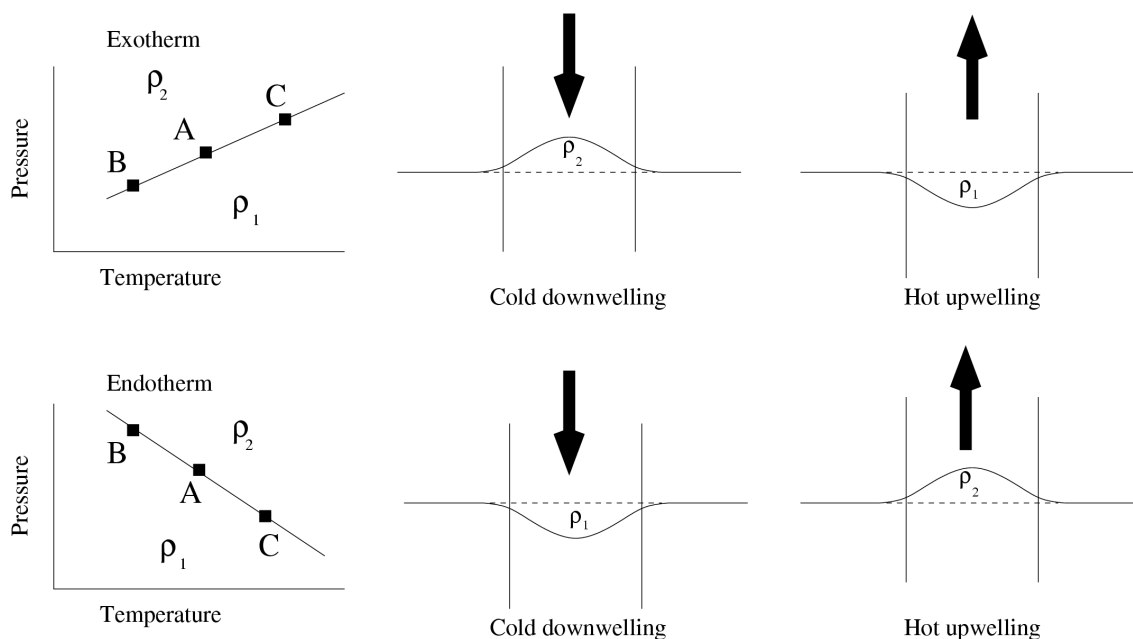


Figure 14: Schematic diagram illustrating the opposite dynamical effect of exothermic- (top row) and endothermic phase transitions (bottom row) on large scale mantle circulation. The left hand column shows the schematic phase diagrams for the two exothermic/endothermic cases with pressure and temperature increasing in the upward and left to right direction respectively. The Clapeyron curves are shown of the two phase transitions with three reference points corresponding to a reference background  $P, T$  position of the phase boundary (A) and the  $P, T$  position (B) in a cold downwelling (lithospheric slab) or hot upwelling (C) (mantle plume). The high pressure phase has a higher density  $\rho_2 > \rho_1$ . The other two columns illustrate laterally confined vertical flows corresponding to either a cold downwelling or a hot upwelling. Due to the local temperature perturbation associated with the vertical flow the phase boundary shifts vertically from its equilibrium position, indicated by the dashed line.

These effects are illustrated in the diagram in Fig. 14. In cold downwelling slabs crossing an exothermic phase boundary with a positive Clapeyron slope,  $\gamma = dP/dT > 0$ , the cold perturbation represented by the slab ( $\delta T < 0$ ) causes the phase boundary to shift upwards, to lower pressure, ( $\delta P < 0$ ), thereby creating a positive density anomaly,  $\delta\rho = \rho_2 - \rho_1 > 0$ , in the region enclosed by the uplifted boundary. This increases the negative buoyancy of the downwelling flow and re-enforces the circulation. A similar situation exists for an exothermic phase boundary and a hot upwelling flow, such as in a hypothetical hot mantle plume. Here the phase boundary is shifted to a higher pressure, creating a negative density anomaly,  $\delta\rho = \rho_1 - \rho_2$ , and positive buoyancy which enforces the upward flow.

For endothermic phase boundaries with a negative Clapeyron slope the situation is opposite and both cold downwellings and hot upwellings experience resisting body forces related to a negative density anomaly in a cold downwelling and a positive anomaly in a hot upwelling.

From this analysis it follows that an endothermic phase transition forms an obstacle for whole mantle convection. It has been found that the tendency towards layered convection in the presence of an endothermic phase transition increases with the Rayleigh number (Christensen and Yuen, 1984). The efficiency of convective heat transport decreases in case of layered convection and it follows that in the early Earth when the effective Rayleigh number was higher the effect of the endothermic phase boundary has been to slow down convective cooling of the mantle.

The effect of the endothermic phase boundary near 660 km depth is illustrated in Fig. 15, showing results of a numerical modelling experiment. This figure shows a snapshot of the distribution of mineral phase and temperature for a 2-D rectangular, time dependent convection model including three different mineral phases.

The phases shown in the top frame are: blue olivine(spinel) green postspinel (perovskite plus periclase) and red postperovskite plus periclase. The postperovskite structures near the bottom coincide with colder regions, interrupted by hot plumes rising from the core mantle boundary shown in the bottom frame. The contour lines illustrate the instantaneous flow velocity. Note that the topography of the 660 km phase boundary correlates with the local temperature in agreement with the schematic phase diagram in Fig. 14. Apparently cold downwellings sometimes cross the 660 km phase boundary directly in some regions, whereas in other locations deflection of slab like structures can occur at the phase boundary, in agreement with images of seismic tomography (Albarede and van der Hilst, 2002).

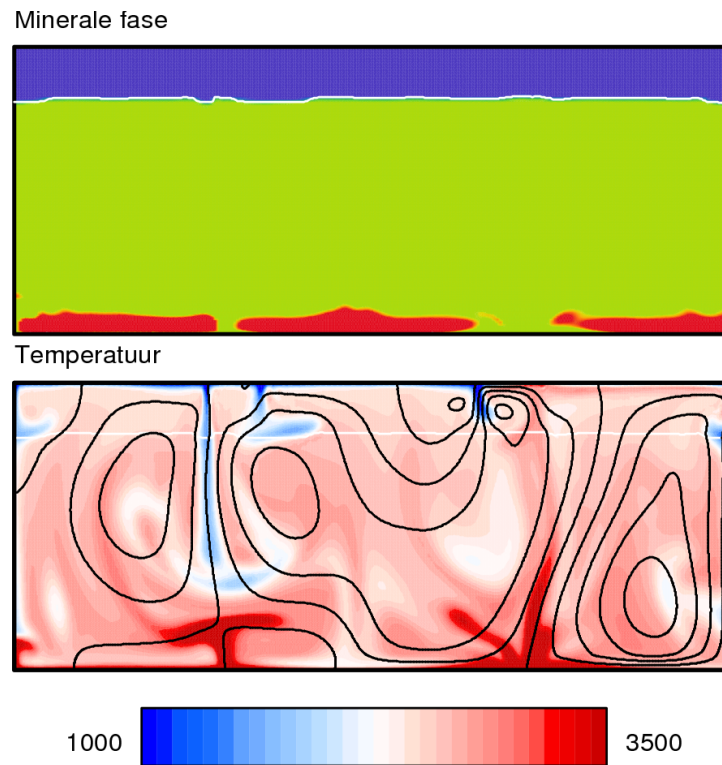


Figure 15: Snapshot from a time dependent convection model showing mineral phase and temperature. The phases shown in the top frame are: blue olivine (spinel) green postspinel (perovskite plus periclase) and red postperovskite plus periclase. The white line marking the spinel to postspinel boundary defines the boundary between the upper and lower mantle near 660 km depth. The irregular structures near the bottom are regions occupied by the high pressure postperovskite phase.

## References

- [1] Albarede, F. and R.D. van der Hilst, Zoned mantle convection, *Philosophical Transactions of the Royal Society of London*, Series A-Math.Phys. and Engineering sciences 360 (1800), 2569-2592, Nov.15 2002.
- [2] Anders, E. and N. Grevesse, Abundances of the elements: Meteoritic and solar, *Geochimica et Cosmochimica Acta*, **53**, 197-214, 1989.
- [3] Birch, F., Elasticity and constitution of the Earth's interior, *J. geophys. Res.*, **57**, 227-286, 1952.
- [4] Boehler, R., Melting temperature of the Earth's mantle and core: Earth's thermal structure, *Annu. Rev. Earth Planet. Sci.*, 24, 15-40,1996.
- [5] Brown, G.C. and A.E. Musset, *The inaccessible Earth*, (second edition), Chapman & Hall, 1993.
- [6] Buffett, B.A., The thermal state of the Earth's core *Science*, **299**, 789-791, 2003.
- [7] Bullen, K.E., *The earth's density*, Chapman and Hall, London, 1975.
- [8] Bunge, H-P., Ricard, Y. and J. Matas, Non-adiabaticity in mantle convection, *Geophys. Res. Lett.*, **28**, 5, 879-882, 2001.
- [9] Christensen, U.R. and D.A. Yuen, Layered convection induced by phase transitions, *J. Geophys. Res.*, **90**, 10291-10300, 1985.
- [10] Dziewonski, A.M. and D.L. Anderson, Preliminary reference earth model (PREM), *Phys. Earth Planet. Int.*, **25**, 297-356, 1981.
- [11] Hemley, R.J., Erskine Williamson, extreme conditions and the birth of mineral physics, *Physics Today*, April 2006, 50-57.
- [12] J.W. Hernlund, C. Thomas, P.J. Tackley, A doubling of the post-preovskite phase boundary and structure of the Earth's lowermost mantle, *Nature*, **434**, 882-886, 2005.
- [13] Hirose, K., Post-Perovskite phase transition and the nature of the D" layer, in: *Superplumes: beyond plate tectonics*, 69-82, Ed. D.A. Yuen, S. Maruyama, S-I. Karato and B.F. Windley, Springer, 2007.
- [14] Hofmeister, A.M., Mantle values of thermal conductivity and the geotherm from phonon lifetimes, *Science*, **283**, 1699-1706, 1999.
- [15] Holmes, A., Radioactivity in the Earth and the Earth's thermal history, *Geol. Mag.*,**2**, 60-71 and 102-112, 1915.
- [16] Jacobs, M.H.G. and B.H.W.S. de Jong, Placing constraints on phase equilibria and thermo-physical properties in the system MgO – SiO<sub>2</sub> by a thermodynamically consistent vibrational method, *Geochimica et Cosmochimica Acta*, **71**, 3630-3655, 2007.
- [17] Jackson, M.J. and H.N. Pollack, On the sensitivity of parameterized convection to the rate of decay of internal heat sources, *J. Geophys. Res.*, **89**, 10,103-10,108, 1984.

- [18] Kellog, L.H., Hager, B.H. and R.D. van der Hilst, Compositional stratification in the deep mantle: Towards a hybrid convection model, *Science*, 283, 1881-1884, 1999.
- [19] Lay, T., Heinz, D., Ishii, M., Shim, S-H., Tsuchiya, J., Tsuchiya, T., Wentzcovitch, R. and D. Yuen, Multidisciplinary Impact of the deep mantle phase transition in perovskite structure, *EOS, TRANSACTIONS, AMERICAN GEOPHYSICAL UNION*, **86**, No. 1, 2005.
- [20] Loper, D.E., The gravitationally powered dynamo, *Geophys. J. R. astr. Soc.*, **54**, 389-404, 1978.
- [21] MacDonald, G.J.F., *Chondrites and the chemical composition of the Earth*, in: Researches in Geochemistry, ed. P.H. Abelson, **1**, 476-494, Wiley, New York, 1959.
- [22] Malvern, L.E., *Introduction to the mechanics of a continuous medium*, Prentice-Hall, Englewood Cliffs, New Jersey, 1969.
- [23] Matyska, C. and D.A. Yuen, Profiles of the Bullen parameter from mantle convection modelling, *Earth Planet. Sci. Lett.*, **178**, 39-46, 2000.
- [24] McBride, N. and I. Gilmour, *An introduction to the solar system*, Cambridge University Press, 2003.
- [25] Poirier, J-P, *Introduction to the Physics of the Earth's Interior*, (second edition), Cambridge University Press, 2000.
- [26] Pollack, H.N. *Thermal characteristics of the Archaean*, in: Greenstone Belts, ed.: M.J. de Wit, L.D. Ashwal, Oxford University Press, 1997.
- [27] Pollack, H.N., Hurter, S.J. and J.R. Johnson, Heat flow from the earth's interior: analysis of the global data set, *Reviews of Geophysics*, **31**, 267-280, 1993.
- [28] Rama Murthy, V., van Westrenen, W. and Y. Fei, Experimental evidence that potassium is a substantial radioactive heat source in planetary cores, *Nature*, **423**, 163-165, 2003.
- [29] Schubert, G., Stevenson, D. and P. Cassen, Whole planet cooling and the radiogenic heat source content of the earth and moon, *J. Geophys. Res.*, **85**, 2531-2538, 1980.
- [30] Spengler, D., van Roermund, H.L.M., Drury, M.R., Ottolini, L., Mason, P.R.D. and G.R. Davies, Deep origin and hot melting of an Archaean orogenic peridotite massif in Norway, *Nature*, **440**, 2006. doi:10.1038/nature04644
- [31] Stixrude, L. and Carolina Lithgow-Bertelloni, Thermodynamics of mantle minerals - I. Physical properties, *Geophys. J. Int.*, **162**, doi: 10.1111/j.1365-246X.2005.02642, 610-632, 2005.
- [32] Tozer, D.C., The present thermal state of the terrestrial planets *Phys. Earth Planet. Inter.*, **6**, 182-197, 1972.
- [33] Turcotte, D.L., and G. Schubert, *Geodynamics* (second edition), Cambridge University Press, 2001.
- [34] van den Berg, A.P., Rainey, E.S.G. and D.A. Yuen, The combined influences of variable thermal conductivity, temperature- and pressure-dependent viscosity and core-mantle coupling on thermal evolution *Phys. Earth Planet. Inter.*, **149**, 259-278, 2005.

- [35] van den Berg, A.P. and D.A. Yuen, Modelling planetary dynamics by using the temperature at the core-mantle boundary as a control variable: effects of rheological layering on mantle heat transport, *Phys. Earth Planet. Inter.*, **108**, 219-234, 1998.
- [36] van der Hilst, R.D., de Hoop, M.V., Wang, P., Shim, S.-H., Ma, P. and L. Tenorio, Seismostratigraphy and thermal structure of Earth's core-mantle boundary region, *Science*, **315**, 1813-1817, 2007.
- [37] van Hunen, J. and A.P. van den Berg, Plate tectonics on the early Earth: limitations imposed by strength and buoyancy of subducted lithosphere, *Lithos*, **103**, 217-235, 2008.
- [38] van Thienen, P., Vlaar, N.J. and A.P. van den Berg, Plate tectonics on the terrestrial planets *Phys. Earth Planet. Inter.*, **142**, 61-74, 2004.
- [39] Vlaar, N.J. and A.P. van den Berg, Continental evolution and archaeo-sea-levels, in: *Glacial Isostasy, Sea-Level and Mantle Rheology*, 637-662, ed. R. Sabadini, K. Lambeck, E.V. Boschi, Kluwer academic publishers, 1991.
- [40] N.J. Vlaar, P.E. van Keken, A.P. van den Berg, Cooling of the Earth in the Archaean: consequences of pressure-release melting in a hotter mantle, *Earth and Planetary Science Letters*, **121** 1-18, 1994.
- [41] Williamson E.D. and L.H. Adams, Density distribution in the Earth, *Journal of the Washington academy of sciences*, **13**, 413-428, 1923.

# Appendix

## A Concepts of thermal energy transport

In this appendix the energy transport equations, that are used in the thermal evolution models introduced in the main text are summarized.

We consider the evolution of a temperature field controlled by convection/diffusion processes in a 3-D spatial configuration.

### A.1 Transport equations

The temperature is described as a scalar field  $T(x, y, z, t)$  of the space ( $\mathbf{x} = (x, y, z)$ ) and time ( $t$ ) coordinates. The temperature gradient is defined as  $\nabla T = (\partial T/\partial x, \partial T/\partial y, \partial T/\partial z)$ . The main transport mechanisms of thermal energy considered are:

#### 1. Conductive transport

In a general formulation of diffusion processes by Fourier's (Fick) law, a flux density vector  $\mathbf{J}$  is expressed in terms of the thermal gradient and the thermal conductivity,

$$\mathbf{J} = -k\nabla T \quad (100)$$

where in general, for an anisotropic medium,  $k$  is a conductivity tensor with  $J_i = -k_{ij}\partial_j T$ . We will assume an isotropic medium here with  $k_{ij} = k\delta_{ij}$ , and scalar conductivity  $k$ .

The energy transport equation for a purely conductive case follows from an energy conservation principle applied to a control volume  $V$  in a static (non-deformable) medium,

$$\frac{d}{dt} \int_V \rho c_P T dV = - \int_A \mathbf{J} \cdot \mathbf{n} dA + \int_V H_v dV \quad (101)$$

$\rho$  and  $c_P$  are density and specific heat and  $H_v = \rho H$  [ $Wm^{-3}$ ] is the (volumetric) density of the internal heating rate.

Differentiating inside the first integral, assuming  $\rho c_P$  constant, substituting (100), and applying the Gauss divergence theorem to the surface integral we get

$$\int_V \rho c_P \frac{\partial T}{\partial t} dV = \int_V \nabla \cdot k \nabla T dV + \int_V H_v dV \quad (102)$$

Since  $V$  is an arbitrary control volume we arrive at the time dependent diffusion equation,

$$\rho c_P \frac{\partial T}{\partial t} = \nabla \cdot k \nabla T + H_v \quad (103)$$

#### 2. General convection/diffusion transport case

For thermal convection models convective energy transport, coupled to mass transport, can be the dominant transport mechanism. In this case the energy flow density contains a convective part

$$\mathbf{I} = -k\nabla T + \rho c_p T \mathbf{u} \quad (104)$$

where  $\mathbf{u}$  is the flow velocity vector field. We assume the medium here to be incompressible, implying a divergence free velocity field  $\nabla \cdot \mathbf{u} = 0$ .

We now apply the energy conservation principle to a static control volume with a permeable closed boundary surface to get,

$$\int_V \rho c_P \frac{\partial T}{\partial t} dV = - \int_A (-k \nabla T + \rho c_P T \mathbf{u}) \cdot \mathbf{n} dA + \int_V H_v dV \quad (105)$$

Applying Gauss theorem to the surface flux term, substituting the incompressibility condition,  $\nabla \cdot \mathbf{u} = 0$ , and assuming  $\nabla(\rho c_P) = \mathbf{0}$ , we get,

$$\rho c_P \frac{\partial T}{\partial t} = \nabla \cdot k \nabla T - \rho c_P \nabla T \cdot \mathbf{u} + H_v \quad (106)$$

Substitution of the material or Langrangian derivative  $\frac{D(\cdot)}{Dt} = \frac{\partial(\cdot)}{\partial t} + \mathbf{u} \cdot \nabla(\cdot)$ , we obtain the convection/diffusion equation for heat transport in a flowing medium,

$$\rho c_P \frac{DT}{Dt} = \nabla \cdot k \nabla T + H \quad (107)$$

## A.2 Thermal energy conservation applied to a cooling body

An approximation of the cooling behavior of a (planetary) body can be obtained from a conservation principle for thermal energy by integrating over the volume  $V = \int_V dV$  with surface  $\partial V$  enclosing the cooling body with surface area  $A = \int_{\partial V} dA$ . Assuming the surface to be impermeable, with  $\mathbf{u} \cdot \mathbf{n} = 0$ , ( $\mathbf{u}$  and  $\mathbf{n}$  are the material flow velocity and outward pointing normal vector on the surface), we have with (101),

$$\frac{d}{dt} \int_V \rho c_p T dV = - \int_{\partial V} q dA + \int_V H_v dV \quad (108)$$

where  $q(x, t) = \mathbf{J} \cdot \mathbf{n}$  is the surface heatflow density. Assuming uniform heat capacity  $C = \rho c_P$  and introducing the volume average values  $\langle T \rangle$ ,  $\langle H \rangle$  and defining  $Q = \frac{1}{V} \int_A q dA$  we get,

$$C \frac{d}{dt} \langle T \rangle = -Q(t) + \langle H_v(t) \rangle \quad (109)$$

(109) is an ordinary differential equation (ODE) for the time dependent volume averaged temperature of the cooling body.

In the literature on planetary thermal evolution the ratio of the instantaneous, global internal heatproduction rate and the surface heatflux is defined as the non-dimensional Urey number,

$$Ur(t) = \frac{\int_V H_v(t) dV}{\int_A q(t) dA} = \frac{\langle H_v \rangle}{\frac{A}{V} \langle q \rangle} = \frac{\langle H_v(t) \rangle}{Q(t)} \quad (110)$$

In general  $q(x, t)$  and hence  $Q(t)$  are not known and assumptions concerning the relation between surface heatflux and internal temperature have to be made in order to make (109) solvable. Several alternative parameterizations of  $Q$  in terms of  $\langle T \rangle$  are discussed in section 3.5.

### A.3 The adiabatic temperature profile of a convecting layer

Often an adiabatic temperature profile is used as a reference for the temperature distribution in the convecting mantle or outer core. The adiabatic nature of the horizontally averaged temperature in a vigorously convecting layer follows from considering a more complete energy transport equation than the approximate Boussinesq formulation (107) (Schubert, Olson and Turcotte, 2001). Derivation of the full equation, including terms corresponding to adiabatic (de)compression and viscous dissipation is outside the scope of this course. Such a derivation can be found (Malvern, 1969). We only give the resulting equation here,

$$\rho c_P \frac{dT}{dt} - \alpha T \frac{dP}{dt} = \partial_j (k \partial_i T) + \Phi + \rho H \quad (111)$$

Here the second term left represents the adiabatic (de)compression, the second term on the righthand side represents the volume density of the power generated by viscous dissipation,  $\Phi = \tau_{ij} \partial_i u_j$ , expressed in the shear stress tensor and the strain rate tensor.  $\rho H$  represents the volumetric heating rate from other sources, such as radiogenic heating.

Using the thermodynamic expression for the entropy differential, and the Maxwell relation  $(\partial S / \partial P)_T = -(\partial V / \partial T)_P$ , we obtain,

$$\begin{aligned} dS &= \left( \frac{\partial S}{\partial T} \right)_P dT + \left( \frac{\partial S}{\partial P} \right)_T dP \\ &= \left( \frac{\partial S}{\partial T} \right)_P dT - \left( \frac{\partial V}{\partial T} \right)_P dP = \frac{c_P}{T} dT - \frac{\alpha}{\rho} dP \end{aligned} \quad (112)$$

it follows that,

$$\rho c_P \frac{dT}{dt} - \alpha T \frac{dP}{dt} = \rho T \frac{dS}{dt} \quad (113)$$

Combining (111) and (113) we arrive at a physical interpretation of heat and mass transport under adiabatic conditions. The adiabatic assumption implies that  $dS/dt = 0$ . From (111) it follows that this condition applies when thermal diffusion, viscous dissipation and internal heating are all negligible. The only remaining transport process is advection, implicit in the material derivative  $d \cdot / dt$ .

From (113) we derive an explicit form of the adiabatic temperature profile,

$$\rho c_P \frac{dT}{dt} - \alpha T \frac{dP}{dt} = 0 \quad (114)$$

or equivalently,

$$\frac{1}{T} dT = \frac{\alpha}{\rho c_P} dP = -\frac{\alpha g}{c_P} dr \rightarrow \int_{T(R)}^{T(r)} \frac{dT}{T} = \ln \left( \frac{T(r)}{T(R)} \right) = - \int_R^r \frac{\alpha g}{c_P} dr' \quad (115)$$

$$T(r) = T(R) \exp \left( - \int_R^r \frac{\alpha g}{c_P} dr' \right) \quad (116)$$

In cases with a uniform *thermal scale height*  $H_T$  defined by  $H_T^{-1} = \alpha g / c_P$  this becomes an exponential temperature profile,  $T(r) = T(R) \exp(H_T^{-1}(R - r)) = T(R) \exp(z/H_T)$ , where  $z$  is the depth coordinate.<sup>20</sup>

<sup>20</sup>See also section 2.6.3 and problem 27.